Topics in Quantum Computation and Information: Entanglement, Noise, and Error Correction

by

Daniel E. Crow

A dissertation submitted in partial fulfillment of
the requirements for the degree of

Doctor of Philosophy

(Physics)

at the

University of Wisconsin–Madison

2016

Date of final oral examination: 08/04/2016

The dissertation is approved by the following members of the final oral committee:

Robert Joynt, Professor, Physics
Mark Saffman, Professor, Physics
Lisa Everett, Professor, Physics
Eric Bach, Professor, Computer Science
Mark Friesen, Senior Scientist, Physics

ABSTRACT

This dissertation explores several topics pertaining to quantum computation and information theory. First, we discuss the distinction between entangled and separable states from a geometric point of view. In particular, we construct the ellipsoid of smallest volume that bounds the set of separable states for systems of n qubits, although the results generalize easily to larger spaces. This ellipsoid serves as an approximation of the boundary between separable and entangled states. Notably, we show that when restricted to pure states all separable states lie on the ellipsoid boundary, and all entangled states lie outside. We demonstrate that this distinguishing power motivates an entanglement measure on pure states. For 2 qubits, this measure can be written in a particularly convenient form, while for 3 or more qubits the ellipsoid structure provides a natural weighting of entanglement shared between subsystems of varying size.

We then address classical models of quantum noise. Though the classical noise models are not fully general, it is known that certain classes of quantum noise can be realized classically. In particular, dephasing noise can always be simulated classically. For a single qubit, we explicitly construct classical models to simulate arbitrary dephasing noise. For two qubits, we construct classical models that reproduce a subset of the dephasing noise; these models can be combined to create more complicated dephasing behavior. Additionally, we show that depolarizing noise is classical for quantum systems of arbitrary dimension.

Lastly we discuss error correction. Motivated by experimental capabilities and limitations of neutral atom qubits, we explore the practical possibility of measurement-free error correction. For three well known error correction codes—the bit-flip, Bacon-Shor, and Steane codes—we adapt standard measurement-based procedures to measurement-free circuits on neutral atom systems. In particular, we present a novel syndrome extraction technique to achieve fault-tolerance. Using numerical simulation we estimate first-level depolarizing thresholds for these circuits. We find that simulating realistic conditions for the bit-flip, Bacon-Shor, and Steane codes produced error thresholds of $p_{\text{th}} \approx 10^{-2}$, 10^{-3}, and 10^{-4}, respectively. Encouragingly,

these results are within the range of expected neutral atom capabilities and compare well to measurement-based threshold values.

ACKNOWLEDGMENTS

First I thank my advisor, Robert Joynt. My work constantly benefited from his guidance, assistance, and insight. I also thank him for his warmth and generosity outside of school, helping to make my time in graduate school more pleasant.

I thank Mark Saffman, for providing the inspiration for the error correction portion of this work, his valuable collaboration on that project, and his general support throughout my time here.

I am also grateful to my collaborator David Dynerman, who provided tremendous help with our project on the geometry of entangled states, as well as his frequent guidance with a wide range of math, programming, and peripheral questions.

Many faculty also deserve thanks for their help with research, serving on committees, as course instructors, and other aspects of my graduate school career. In particular, I am grateful to Susan Coppersmith, Mark Friesen, Eric Bach, Lisa Everett, and Michael Winokur.

For a variety of physics, math, and programming related discussions that directly or indirectly influenced me, I thank Kenneth Rudinger, Todd Garon, Neil Baron, William Cottrell, Josh Isaacs, Adam Frees, James Hanson, Joydip Ghosh, Ekmel Ercan, Gerardo Paz-Silva, Ben Stefanek, Jason Milhone, Ken Flanagan, and Tom Perry. Additionally, I'd like to thank the physics department staff for their regular assistance, but especially Renée Lefkow.

I am grateful for unwavering encouragement from by parents, brother, and sister. The same holds for my extended family, although I would particularly like to thank the Madison branch for making me feel at home in Wisconsin. Additionally, I am grateful for the various scientists and mathematicians in my family who have served as mentors and inspirations throughout my life.

Lastly, I thank my friends that have supported me in many ways, academically and otherwise.

CONTENTS

LIST OF FIGURES

LIST OF TABLES

1 INTRODUCTION

Although quantum computing was first proposed by Richard Feynman in the 1980s, only with the discovery of quantum error correction by Peter Shor in 1995 was it viewed as a practical possibility. In the roughly 20 years since, research in the field has expanded dramatically. From the theoretical point of view, information, algorithms, and error correction have all seen dramatic progress. Experimentally, quantum bits have been realized on a variety of platforms but we have yet to create a fully protected logical qubit. Significant work remains to be done to realize a functional quantum computer.

In this work, we explore several topics related to quantum computation and information theory. We first examine the distinction between separable and entangled states from a geometric point of view. Second, we compare classical and quantum noise models, providing explicit constructions of classical models equivalent to certain classes of quantum models. Lastly, we look at error correction—in particular, we address some of the challenges associated with implementing error correction using neutral atomic qubits.

1.1 Document outline

The content is divided into three chapters. Chapter 2 covers the geometry of separable (non-entangled) states, Chapter 3 covers quantum noise, and Chapter 4 covers error correction.

Chapter 2 begins with a general summary of the geometry of quantum states that will also be useful in later chapters. We then address the problem of distinguishing entangled and separable states. This problem is much studied and highly nontrivial—in general the problem is NP-complete. Rather than solving the problem exactly, we attempt to approximate the set of separable states using techniques from algebraic geometry. We provide a review of the relevant mathematics which we then use to construct the minimum-volume ellipsoid that bounds the set of separable

states, approximating the boundary between separable and entangled states and providing insight about the geometry. We assess the tightness of this ellipsoid and its distinguishing power, showing that when restricted to pure states the boundary can perfectly determine separability. Lastly, we show that when restricted to pure states, this structure gives rise to an entanglement measure.

In Chapter 3, we construct classical noise models that simulate certain classes of quantum noise. Thus, we begin with a review of noise models, both quantum and classical. We then look at three cases of simulating quantum noise with classical models, beginning with single-qubit dephasing noise. Restricted to this case, we show that all dephasing noise can be explicitly constructed and we calculate such models explicitly for several well-known quantum noise models. Somewhat surprisingly, we see that these classical noise models can reproduce behavior that is typically viewed as distinctly quantum, such as recoherence. We then assess dephasing for the 2-qubit case, where we construct classical realizations of a subset of dephasing noise models. Lastly, we examine depolarizing noise for an N-dimensional quantum system, demonstrating a classical model to reproduce depolarizing noise for arbitrary dimension [1].

Chapter 4 focuses on error correction. Error correction is a necessary technique for reliably storing and processing quantum information. In the typical error correction paradigm, measurement is used as a frequent resource. This poses a difficulty for neutral atom qubits which must avoid measurement during computation. Thus error correction techniques must be adapted to work without measurement. We address the difficulty using a novel syndrome extraction technique. This technique is particularly well-suited for neutral atoms, which can in principle implement multiqubit logic gates for reasonably large numbers of qubits [2].

The chapter begins with a review of standard error correction theory and examples of three well-known error correction codes. We then introduce the technique of using additional stabilizers to detect syndrome extraction errors, which is relevant to both measurement-free and measurement-based error correction. Continuing with the example codes, we show how this technique can be used with neutral atom resources to create fault-tolerant, measurement-free error correction circuits.

To analyze the performance of these circuits, we performed numerical simulation to determine the error thresholds for each of the three example codes. We provide a description of the simulation techniques and we summarize the results. The threshold values demonstrate significant improvement compared to earlier measurement-free results. Additionally—and somewhat surprisingly—we also find that the thresholds are quite reasonable compared to measurement-based thresholds for the same codes.

2 APPROXIMATING THE GEOMETRY OF SEPARABLE QUANTUM STATES

2.1 Introduction

In quantum mechanics, physical systems are represented by wavefunctions, i.e. vectors in complex Hilbert space V. For this entire document, we will use the term vector space interchangeably with Hilbert space. We will also assume that all state vectors have unit length. Suppose two physical systems are described by states in two vector spaces V_1 and V_2 of dimension n and m, respectively. Accounting for the unit norm and irrelevant global phase, the set of valid state vectors for V_1 and V_2 have complex dimension $n-1$ and $m-1$.

A particularly rich feature of quantum mechanics becomes apparent when considering two interacting systems. The combination of these two systems is described by the tensor product $V_1 \otimes V_2$, with dimension nm, or a corresponding set of states with dimension $nm-1$. If we have states $|\psi_1\rangle$ in V_1 and $|\psi_2\rangle$ in V_2, then the combined state is the *product state* $|\psi_1\rangle \otimes |\psi_2\rangle = |\psi_1\rangle\,|\psi_2\rangle$. The set of all such states has dimension $(n-1)+(m-1) < nm-1$. That is, some states in $V_1 \otimes V_2$ can not be written as a product, but can instead only be written as a linear combination of product states.

A state that cannot be written as a product is called *entangled*. Entanglement is a distinctly quantum phenomenon, and arises as both a resource and a nuisance in processing quantum information. As a resource, the precise role of entanglement is subject to a fair amount of debate [3–6]. However, a reasonable conclusion is perhaps that for any practical quantum computation, entanglement is probably necessary. Entanglement also shows up as our information-processing system becomes entangled with its environment, leading to *quantum noise* and *decoherence* (see Chapter 3). Furthermore, our best strategies to combat such noise depend on maintaining highly entangled states (see Chapter 4).

Despite a substantial amount of work on the subject, entanglement remains particularly difficult to describe. In fact, the problem of determining whether a

given state is entangled has been shown to be NP-complete [7, 8]. However, this result does not mean that hope is lost. Certainly, in a variety of important simple cases, determining whether or not a state is entangled is quite easy. Here, we seek to approximate the set of entangled states using mathematical results on the theory of orbitopes.

2.2 Geometry of quantum states

The set of states of a quantum system has a rich geometric structure. This discussion will be helpful for subsequent chapters as well, so we will describe the general geometry before focusing on entanglement.

State vectors as projection operators

An N-dimensional quantum system is described by rays in the projective Hilbert space $\mathbb{CP}^{N-1}$. Typically, we represent these rays by unit vectors in the space

$$H = \mathbb{C}^N$$

and take two vectors to be equivalent if they satisfy $|\psi\rangle = e^{i\phi} |\psi'\rangle$ with θ real. That is, states are not uniquely defined as vectors.

For a normalized state $|\psi\rangle$, consider the operator

$$\rho = |\psi\rangle \langle\psi| .$$

The operator ρ is the projection operator onto $|\psi\rangle$. Note that $\operatorname{Tr} \rho = 1$ and $\rho^2 = \rho$. An operator ρ of this form is called a rank-1 projector, and each such operator uniquely determines a ray in $\mathbb{CP}^{N-1}$. To see the invariance with respect to global phase, note that for a state $|\psi'\rangle = e^{i\theta} |\psi\rangle$ we have

$$|\psi'\rangle \langle\psi'| = e^{i\theta} |\psi\rangle \langle\psi| e^{-i\theta} = |\psi\rangle \langle\psi| = \rho.$$

For two states $|\psi\rangle$ and $|\phi\rangle$ that differ by more than a global phase, note that

$$\mathrm{Tr}(\rho_\psi \rho_\phi) = \mathrm{Tr}(|\psi\rangle \langle\psi| \, \phi\rangle \langle\phi|) = \mathrm{Tr}(\langle\phi| \, \psi\rangle \langle\psi| \, \phi\rangle) = ||\langle\psi| \, \phi\rangle||^2 .$$

Additionally, unitary evolution is also easily formulated for these operators as

$$U |\psi\rangle \to U \rho U^\dagger$$

while expectation values of a Hermitian operator O are given by

$$\langle\psi| \, O \, |\psi\rangle = \mathrm{Tr}(\rho \cdot O).$$

Thus, the projection operators of this form easily reproduce the fundamental tools needed for state vector quantum mechanics.

Unfortunately, the state vector picture has a notable deficiency. That is, two interacting systems can create states such that we can no longer adequately describe the individual subsystems using state vectors. For example, consider the state $|\psi\rangle$ in $V_A \otimes V_B$ given by

$$|\psi\rangle = \frac{1}{\sqrt{2}} |0\rangle |0\rangle + \frac{1}{\sqrt{2}} |1\rangle |1\rangle$$

where V_A and V_B are two distinct but isomorphic 2-dimensional systems, each spanned by basis vectors labeled $|0\rangle$ and $|1\rangle$. A natural question is, "What is the state of subsystem A?" It turns out that system A cannot be described by a state vector. However, we can describe system A using an ensemble, or a classical probability distribution over the set of state vectors in V_A. These ensembles are naturally described by generalizing the projection operators to *density operators*.

Density operators

The idea of generalizing state vectors to density operators was introduced independently by von Neumann and Landau, both in 1927. Landau introduced the idea as a way to deal with decoherence that arises as a system interacts with its environ-

ment, while von Neumann used them to deal with ensembles in statistical mechanics. Conveniently, the same formalism handles both cases.

Here we will use ensembles to motivate the definition. First, note that diagonal entries in a matrix $|\psi\rangle\langle\psi|$ represent probabilities rather than amplitudes. Since classical probabilities can be combined via convex combination, a natural guess is to try taking convex combinations of projection operators.

We define density operators as the convex hull of all rank-1 projectors. That is, an arbitrary density matrix can be written as the convex combination

$$\rho = \sum p_i \, |\psi_i\rangle\langle\psi_i|$$

with $0 \leq p_i \leq 1$ and $\sum p_i = 1$. In some sense this can be interpreted as corresponding to the ensemble $\{(\, p_i, \, |\psi_i\rangle\,)\}$, but this decomposition is not unique in general. A density operator ρ acting on H is positive semi-definite and satisfies

$$\operatorname{Tr}\rho = 1.$$

Equivalently, ρ is Hermitian and has eigenvalues p_i satisfying $0 \leq p_i \leq 1$ and $\sum p_i = 1$. Thus it holds that

$$\operatorname{Tr}\rho^2 \leq 1,$$

with equality holding for *pure states.* The pure states are the rank-1 projectors and are in one-to-one correspondence with the state vectors, up to overall phase. A state that is not pure is called *mixed*, although this term is also used to refer to a general quantum state.

Bloch Coordinates

Here we restrict to 2-dimensional quantum systems, or qubits. We will take $|0\rangle$ and $|1\rangle$ to be an orthonormal basis for each qubit. Thus, single qubit states are described by a 2×2 density matrices, which can be parameterized in a particularly convenient way.

Recall that the Pauli matrices are given by $\sigma_0 = I_2$ and

$$\sigma_1 = \begin{pmatrix} 0 & 1 \\ 1 & 0 \end{pmatrix}, \quad \sigma_2 = \begin{pmatrix} 0 & -i \\ i & 0 \end{pmatrix}, \quad \sigma_3 = \begin{pmatrix} 1 & 0 \\ 0 & -1 \end{pmatrix}$$

where I_N denotes thes $N \times N$ identity operator. These operators satisfy $\operatorname{Tr} \sigma_i \sigma_j = 2\delta_{ij}$ and $\operatorname{Tr} \sigma_i = 0$ for $i \neq 0$. These four matrices form an orthogonal basis for 2×2 Hermitian matrices with respect to the trace inner product. Since density operators are Hermitian, we can expand all density matrices in this basis with real coefficients as

$$\rho = \frac{1}{2} \sum v_i \sigma_i. \tag{2.1}$$

From the condition that $\operatorname{Tr} \rho = 1$, we have $v_0 = 1$. The remaining three coefficients form the Bloch vector v in $\mathbb{R}^3$. From the condition that $\operatorname{Tr} \rho^2 \leq 1$ we have $||v|| \leq 1$. That is, the set of all single-qubit states is equivalent to the unit ball in $\mathbb{R}^3$. The $|0\rangle$ state corresponds to the north pole, while $|1\rangle$ corresponds to the south pole. The origin corresponds to the *totally mixed state* which is simply $\rho = \frac{1}{2} I_2$.

The Bloch vector can be easily generalized to n qubits. To do so, we will expand the density matrix in terms of the n-qubit Pauli group, i.e., operators of the form

$$\sigma_{\mathbf{i}} = \sigma_{i_1} \otimes \cdots \otimes \sigma_{i_n}$$

where each σ_{i_j} is a single-qubit Pauli matrix and the subscript $\mathbf{i}$ is shorthand for the full set of indices. As in the single-qubit case, these operators form an orthogonal basis. For n qubits, we define the Bloch vector v according to

$$\rho = \frac{1}{2^n} \left(I + \sum v_{\mathbf{i}} \sigma_{\mathbf{i}} \right) \tag{2.2}$$

where the sum runs over all indices $\mathbf{i} \neq 00 \cdots 0$. Again, the identity term is fixed by the trace condition, leaving a remaining $4^n - 1$ components of the Bloch vector. Occasionally it is convenient to retain the identity component $v_{00\cdots0} = 1$, which we will refer to as the extended Bloch vector.

The n-qubit Bloch vector has a maximum norm given by

$$||v|| \leq \sqrt{2^n - 1}$$

with equality for pure states. Note that unlike the single-qubit case, the set of valid states is not simply the ball with radius $\sqrt{2^n - 1}$, although this set is known to contain a full-dimensional ball [9, 10]. For example, the set of 2-qubit density matrices is 15-dimensional with a 14-dimensional boundary, and the pure states form only a 6-dimensional subset of the boundary. In general, let D_n be the set of valid n-qubit Bloch vectors. The Bloch vector lives in $\mathbb{R}^{4^n-1}$, but D_n is compact and has full dimension so D_n has dimension $4^n - 1$ with boundary of dimension $4^n - 2$. For n qubits, the pure states are given by unit vectors which can be expanded in an orthonormal basis with 2^n elements. Each basis vector provides 2 real degrees of freedom, leaving 2^{n+1} real degrees of freedom. Accounting for unit norm and overall phase leaves $2^{n+1} - 2$ overall real degrees of freedom. Thus, the pure states form only a small subset of the boundary of D_n.

Geometrically, the Bloch coordinates are quite convenient. Unitary rotations of ρ induce orthogonal rotations of the corresponding Bloch vector, and the trace inner product on operators ρ is equivalent to the standard Euclidean inner product on Bloch vectors, up to a constant multiple. In particular, the $SU(2)$ rotations on a single qubit induce $SO(3)$ rotations on Bloch vector v. Note that by considering the extended Bloch vector $\vec{v}$, we have an action of $SO(3)$ on $\mathbb{R}^4$. In this representation, it is clear that the action decomposes into block-diagonal representations of dimension 1 and 3. That is, $\mathbb{R}^4$ decomposes as $1 \oplus 3$ under this action, where 1 is the trivial representation and 3 is the standard 3-dimensional irreducible representation of $SO(3)$. We will discuss representation theory in more detail in Section 2.4.

The Partial Trace

A two-qubit density matrix captures all possible measurement information about the system, including measurements of individual subsystems. Thus, we can construct a single-qubit density matrix corresponding to a single subsystem by ensuring that

measurement outcomes agree. In Bloch coordinates, this simply amounts to the projection $v \to v_A, v_B$ given by

$$v_A = (v_{10}, v_{20}, v_{30}),$$
$$v_B = (v_{01}, v_{02}, v_{03}).$$

In terms of the density matrices themselves, this operation is referred to as the partial trace. To represent this in standard linear algebra notation, let $\{|\psi_i\rangle\}$ and $\{|\phi_j\rangle\}$ be orthonormal bases for V_A and V_B, respectively. Then vectors of the form $|\psi_i\rangle |\phi_j\rangle$ define an orthonormal basis for $V_A \otimes V_B$. Expanding the density matrix in terms of this basis gives

$$\rho_{AB} = \sum a_{ij}^{k\ell} |\psi_i \phi_j\rangle \langle \psi_k \phi_\ell| .$$

Then we can compute the density matrix of subsystem A using the partial trace,

$$\begin{aligned} \rho_A = \mathrm{Tr}_B \, \rho_{AB} &= \sum_{ijk\ell} a_{ij}^{k\ell} |i\rangle \langle k| \langle \phi_\ell | \, \phi_j \rangle \\ &= \sum_{ijk\ell} a_{ij}^{k\ell} |i\rangle \langle k| \, \delta_\ell^j. \end{aligned}$$

For operators that can be written as products, we have

$$\mathrm{Tr}_B \, (O_A \otimes O_B) = \mathrm{Tr}(O_B) \cdot O_A.$$

2.3 Entangled Multiqubit States

An n-qubit state ρ is said to be *separable* if it can be written as a convex combination of product states. That is

$$\rho = \sum_i p_i \cdot (\rho_{i_1} \otimes \cdots \otimes \rho_{i_n})$$

where each ρ_{i_j} is a 2-qubit density operator. Note that if a single-qubit ρ_i is mixed, then ρ_i can be always expanded as a convex combination of two pure states. In the

product for the n-qubit state ρ, replacing each mixed ρ_i with its decomposition into pure states allows us to write an arbitrary separable state as a convex combination of *pure* product states. Thus, we can equivalently *define* separable states as those that can be written as a convex combination of pure product states.

Let D denote the set of all n-qubit density operators, and let S denote the set of separable states. A state ρ is said to be *entangled* if $\rho \in D - S$. It is the boundary between S and $D - S$ that we approximate using the notion of orbitopes, depicted in Fig. 2.1.

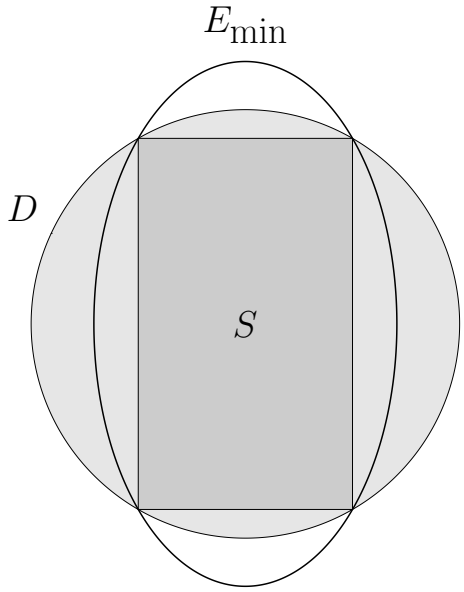

Figure 2.1: The ellipsoid of smallest volume approximates the boundary between separable and entangled states. Here, the set of all density operators is represented as a circle, but note that for 2 or more qubits, this object is contained within a sphere of radius $\sqrt{2^n - 1}$, but is not equal to the sphere.

2.4 Mathematical background

Representation theory

Let G be a group, V be a vector space of dimension N, and M the set of $N \times N$ matrices acting on V. A function f from G to M defines a representation if the function f is a homomorphism, satisfying

$$f(g_1 \cdot g_2) = f(g_1) \cdot f(g_2)$$

for any g_1 and g_2 in G. Since V is N-dimensional, we say that f defines an N-dimensional representation.

Note that the function f defines a group action, so that a group element g acts as a linear transformation on the vectors in V as

$$g \cdot v = f(g) \cdot v.$$

A representation is said to be reducible if the elements $f(g)$ can be written block diagonally in some basis. If no such basis can be chosen, then the representation defined by f is called irreducible, or an irrep. For a reducible representation, V can be decomposed as

$$V = V_1 \oplus \cdots \oplus V_k$$

where $f(g)$ restricted to each component V_i is irreducible. For our purposes, we will need only two irreducible representations of $SU(2)$. First, recall the trivial representation given by $V = \mathbb{R}$ and $f(g) = 1$ for each g. Secondly, $SU(2)$ has a 3-dimensional real representation. By a well-known 2-to-1 mapping, $SU(2)$ maps to the 3-dimensional rotation matrices, $SO(3)$. This mapping defines a 3-dimensional real representation of $SU(2)$. We will denote these simply as 1 and 3. For example, a 7-dimensional representation could decompose as $1 \oplus 3 \oplus 3$.

Note that for products of $SU(2)$, the irreps are simply tensor products of irreducible representations. For example, an irreducible representation of $SU(2) \times SU(2)$ is $3 \otimes 3$.

Orbitopes

Orbitopes, as stated earlier, are the convex hulls of the orbit of a group action on a vector. In our case, the groups that we care about are $SU(2)$ and its products of the form

$$SU(2)^n = SU(2) \times \cdots \times SU(2).$$

Thinking of group elements as operators acting on V, each element g takes a vector v in V to the vector $g \cdot v$. The *orbit* of v under a group action is defined as the set

$$\mathrm{orb}_G(v) = \{g \cdot v \ : \ g \in G\}.$$

For any set X contained in a vector space V, the *convex hull* of X is defined as the set of all convex combinations

$$\mathrm{conv}(X) = \left\{ \sum_i p_i x_i \ : x_i \in X \right\}$$

where $p_i > 0$ and $\sum p_i = 1$. Now returning to the group action of G on a vector v, we can define an orbitope T as

$$T = \mathrm{conv}\left(\mathrm{orb}_G(v)\right).$$

One familiar orbitope is the set of all valid density matrices in N-dimensions, with $G = SU(N)$ and v any pure state. All possible pure states are generated by $SU(N)$ rotations of a given pure state, and mixed states are convex combinations of these pure states.

For our purposes, a more important orbitope is the set of separable states. Recall that a separable state is a convex combination of pure product states. Crucially, all pure product states can be realized via a $SU(2)^n$ action on a single separable pure state.

To demonstrate this fact, let

$$\rho_0 = |00\cdots0\rangle \langle 00\cdots0|.$$

For any single-qubit state $|\phi\rangle$, we can choose an operator U in $SU(2)$ such that $U|0\rangle = |\phi\rangle$. For n qubits, let

$$|\psi\rangle = |\psi_1\rangle\,|\psi_2\rangle\cdots|\psi_n\rangle$$

be an arbitrary pure product state, with corresponding density matrix ρ_ψ. We can choose n unitary operators $\{U_i\}$ such that $U_i|0\rangle = |\psi_i\rangle$. Then we have

$$\rho_\psi = (U_1 \otimes \cdots \otimes U_n)\cdot\rho_0\cdot(U_1 \otimes \cdots \otimes U_n)^\dagger\,.$$

Therefore the set of all pure and separable states is the orbit of ρ_0 under the group action, so the set of all separable states is

$$S = \mathrm{conv}\left(\mathrm{orb}_{SU(2)^n}(\rho_0)\right). \tag{2.3}$$

Bounding orbitopes with ellipsoids

The group action of G on V defines a representation, and can accordingly be decomposed into irreducible subrepresentations. The following mathematical result uses such a decomposition to bound an orbitope within the ellipsoid of smallest volume [11].

Theorem 2.1 (Barvinok-Blekherman)**.** *Let B be the convex hull of a the orbit of a vector $x \in V$:*

$$B = \mathrm{conv}(\mathrm{orb}_G(x)),$$

and assume that B has full dimension in V. The space V can be decomposed into a direct sum of irreducible components V_i:

$$V = \bigoplus_i V_i.$$

Then the smallest volume ellipsoid $E_{\min}$ that contains B is given by

$$E_{\min} = \left\{ v \ : \ \sum_i \frac{\dim V_i}{\dim V} \cdot \frac{||v_i||^2}{||x_i||^2} = 1 \right\}$$

where x_i and v_i are the projections of x and v onto V_i, respectively.

2.5 $E_{\min}$ for separable states

From Eq. 2.3, we can apply the previous theorem to the set of separable states, taking V the space of $2^n \times 2^n$ Hermitian matrices, the group $G = SU(2)^n$, and $x = \rho_0$.

Computing $E_{\min}$

In order to apply Theorem 2.1, we must decompose the action of $SU(2)^n$ into irreducible components. To do this, first consider the action of a single $SU(2)$ acting on single-qubit states. We can write ρ in terms of the extended Bloch vector $\vec{v}$ as

$$\rho = \frac{1}{2} \left(\sigma_0 + v_1 \sigma_1 + v_2 \sigma_2 + v_2 \sigma_3 \right)$$

and as stated earlier, this gives the decomposition get $4 = 1 \oplus 3$. That is, the space of 2-qubit density matrices contains a trivial representation and a 3-dimensional irreducible representation.

For n qubits, we have the semisimple group $SU(2)^n$ whose irreducible representations are n-term tensor products of irreducible representations of $SU(2)$. Fortunately, n-qubit state space is built by taking tensor products of vector spaces that transform according to distinct copies of $SU(2)$. Therefore, in constructing the set of n-qubit density matrices as tensor products of single-qubit operators, we have

$$4^n = (1 \oplus 3)^{\otimes n} = \bigoplus \left(V_{i_1} \otimes \cdots \otimes V_{i_n} \right)$$

where the direct sum in the final expression is taken over all possible products of the

1 and 3 representations.

The space of n-qubit density operators decomposes into irreducible products of the form

$$V = V_{i_1} \otimes \cdots \otimes V_{i_n}$$

with each i_j either 0 or 3 (with V_0 representing the trivial representation). Thus, there are 2^n ways to choose indices, and each occurs exactly once in the decomposition. Each of these is completely determined by the set of indices equal to 3. Since indices with value 0 correspond to trivial representations, the dimension of each irrep is 3^m where m is the number of nonzero indices. Note that the representation determined by all indices equal to 0 gives the trivial representation, which we delete from the final decomposition, leaving a vector space of dimension $4^n - 1$. For the 2-qubit system, the structure can be seen easily by arranging the Bloch components as in Table. 2.1. Observe that there are $\binom{n}{m}$ distinct irreps of dimension 3^m.

Table 2.1: The extended 2-qubit Bloch vector arranged into irreducible representations. The trivial component of the extended Bloch vector is the 00 component. The two 3-component edges form the single-qubit Bloch vectors. The 9-component interior contains the 2-qubit correlations. This generalizes to n-qubits with the Bloch components arranged in an n-dimensional grid.

$1 = v_{00}$	v_{01}	v_{02}	v_{03}
v_{10}	v_{11}	v_{12}	v_{13}
v_{20}	v_{21}	v_{22}	v_{23}
v_{30}	v_{31}	v_{32}	v_{33}

Recall that ρ_0 serves as the vector x in Theorem 2.1. As the final preparation step, we must decompose ρ_0 into its projections onto irreducible components. However, our choice of ρ_0 makes this quite simple. Recall that we have $\rho_0 = |00\cdots0\rangle\langle00\cdots0|$. As a matrix, the single-qubit $|0\rangle$ state is given by

$$|0\rangle\langle0| = \begin{pmatrix} 1 & 0 \\ 0 & 0 \end{pmatrix} = \frac{1}{2}(\sigma_0 + \sigma_3).$$

We get the n-qubit state ρ_0 by taking the n-fold tensor product of the previous expression. Thus, we get

$$\rho_0 = \frac{1}{2^n} (\sigma_0 + \sigma_3)^{\otimes n} .$$

In terms of the Bloch vector,

$$\rho_0 = \frac{1}{2^n} \left(I + \sum v_{i_1 \cdots i_n} \sigma_{i_1 \cdots i_n} \right)$$

we get

$$v_{i_1 \cdots i_n} = \begin{cases} 1, \text{ if } i_k = 0 \text{ or } i_k = 3 \text{ for all } i_k \\ 0, \text{ otherwise.} \end{cases} \tag{2.4}$$

For example, in the 2-qubit case we have

$$v_{00} = v_{03} = v_{30} = v_{33} = 1$$

and all other components equal zero. We see that each irreducible representation has exactly 1 nonzero component, since restricting to a product of $V_3^{\otimes m}$, the only diagonal operator is $Z^{\otimes} m$. so the projection onto each irreducible component satisfies $||v_i|| = 1$. Applying Theorem 2.1, we find that for the n-qubit separable states, the minimum volume bounding ellipsoid $E_{\min}$ is given in Bloch coordinates as

$$E_{\min} = \left\{ v \ : \ \sum \alpha_{i_1 \cdots i_n} v^2_{i_1 \cdots i_n} = 1 \right\} \tag{2.5}$$

where the coefficients are given by

$$\alpha_{i_1 \cdots i_n} = \frac{3^m}{4^n - 1}$$

where m is the number of non-zero indices of α.

For a single qubit, this simply produces the unit ball in $\mathbb{R}^3$, equal to the set of all

states. For the two-qubit case, we can write $E_{\min}$ as

$$\frac{1}{5}\sum_{i\neq 0} v_{i0}^2 + \frac{1}{5}\sum_{j\neq 0} v_{0j}^2 + \frac{3}{5}\sum_{i,j\neq 0} v_{ij}^2 = 1.$$

For three qubits, we get

$$\frac{1}{21}\sum_{m=1} v_{ijk}^2 + \frac{1}{7}\sum_{m=2} v_{ijk}^2 + \frac{3}{7}\sum_{m=3} v_{ijk}^2 = 1$$

where each sum is taken over all components of the m-qubit representations.

Assessing the tightness of $E_{\min}$

To assess how well the ellipsoid bounds the separable states, we first consider just the pure states. For these states we can show that all separable states lie on the ellipsoid, while all entangled states are outside the ellipsoid. That is, the ellipsoid perfectly distinguishes entangled pure states from separable pure states. To see this, it is helpful to define the function

$$b(\rho) = -1 + \sum \alpha_{i_1\cdots i_n} v_{i_1\cdots i_n}^2 \tag{2.6}$$

where the v are the Bloch coordinates of ρ. This function acts as an indicator, with $b(\rho) = 0$ if ρ is on the boundary of $E_{\min}$, $b(\rho) < 0$ if ρ is inside, and $b(\rho) > 0$ if ρ is outside. Thus, states for which $b(\rho)$ is positive are necessarily entangled. Note that $b(\rho)$ is invariant under the group action of $SU(2)^n$, since all such rotations preserve magnitudes in irreducible components.

Starting with a separable state $|00\cdots 0\rangle \leftrightarrow \rho_0$, we can compute $b(\rho_0)$. Since the magnitude of the Bloch vector projected onto each irreducible component is exactly 1, we have

$$b(\rho_0) = -1 + \sum_{m=1}^{n} \binom{n}{m} \left(\frac{3^m}{4^n - 1}\right) = 0. \tag{2.7}$$

Thus, ρ_0 lies on the boundary and by invariance of the group action, it immediately

follows that all separable pure states lie on the boundary.

To see that pure, entangled states lie outside the ellipse, first recall that a pure n-qubit state has a Bloch vector of fixed magnitude, $||v|| = \sqrt{2^n - 1}$. Additionally recall that a pure state is separable if and only if all single-qubit reduced density operators are pure. This is equivalent to the condition that the projection of v onto each $m = 1$ representation must have norm 1. Note that for all valid states, any such projection $v_{m=1}$ satisfies $||v_{m=1}|| \leq 1$.

Now observe that the α coefficients are smallest for the $m = 1$ components of the Bloch vector, since these representations have the lowest dimension. Call this α_1. Then for we can rewrite the sum in Eq. 2.6 as

$$b(\rho) = \alpha_1 ||v|| + \sum \alpha'_{i_1 \cdots i_n} v^2_{i_1 \cdots i_n}$$

where the sum runs over all terms with 2 or more non-zero indices and $\alpha' = \alpha - \alpha_1$. The first term is constant for any pure state. Consider rotating a pure separable state to a pure entangled state. For the initial state, the projection of the Bloch vector onto each subrepresentation has norm 1. For the entangled state, at least two single-qubit Bloch vectors must have norm less than 1. But since the norm of the entire Bloch vector stays constant, the norm in at least one $m > 1$ representation must have norm greater than 1. Thus, the second term in the above sum must increase, and all entangled states must lie *outside* $E_{\min}$.

Since all entangled pure states lie outside the ellipsoid, $b(\rho)$ acts as a measure of entanglement, taking a value greater than 0 only if ρ is definitely entangled. The values of $b(\rho)$ for several well known states are listed in Table 2.2.

For mixed states, the situation is less clear. Certainly, there are mixed entangled states within the ellipsoid. We could attempt to compare the volume of this ellipsoid to the set D_n, although this turns out not to be very helpful. To see why, note that in the 2-qubit case, consider where the ellipse intersects the single-qubit v_{10} axis. With coefficient $\alpha_{10} = 1/5$, the ellipse intersects the axis at $v_{10} = \sqrt{5}$, which is outside the $\sqrt{3}$ maximum radius of 2-qubit Bloch vectors. In 15 dimensions, this extra volume is quite substantial and the volume of the 2-qubit $E_{\min}$ is actually larger than the

Table 2.2: Values of $b(v)$ for several well known entangled states. Wavefunctions are given up to normalization. In the final row, W_{AB} represents the state obtained by tracing out the third qubit (C) from the W state, leaving the 2-qubit AB-subsystem in a mixed state.

		$b(\rho)$
Bell	$\|00\rangle + \|11\rangle$	0.8
GHZ	$\|000\rangle + \|111\rangle$	1.1
W	$\|001\rangle + \|010\rangle + \|100\rangle$	1.0
W_{AB}	$\mathrm{Tr}_C\, \rho_W$	0.22

entire set D_2. Thus, determining the ability of $E_{\min}$ to distinguish mixed states is a nontrivial question. Note that for the 3-qubit W state $|001\rangle + |010\rangle + |100\rangle$, tracing out the third qubit leaves a 2-qubit entangled mixed state that lies outside $E_{\min}$.

Using $b(\rho)$ as an entanglement measure

The ability of $b(\rho)$ to distinguish pure from entangled states suggests that it can be used as an entanglement measure. Entanglement measures are defined in a variety of ways. In general, a valid entanglement measure satisfies two important properties. Let $\mu(\rho)$ be a real-valued function. For convenience, assume $\mu(\rho) = 0$ for separable ρ. An entanglement monotone [12] satisfies the following properties:

1. $\mu(\rho)$ does not increase under local operations.
2. $\mu\left(\sum p_i \rho_i\right) \leq \sum p_i \mu(\rho_i)$.

The first condition includes all operations that can be performed locally, including measurement and discarding qubits. The second condition expresses the condition that entanglement cannot be increased by mixing states. Demonstrating that $b(\rho)$ satisfies these properties is straightforward, so b is a valid entanglement monotone. In principle, there are infinitely many entanglement monotones for a given system. However, a particularly convenient property of b is that it is simple to calculate, as opposed to

many such monotones that require minimization over possible convex combinations. On the other hand, $b(\rho)$ is not capable of distinguishing certain entangled states. We can define a more sensitive, albeit more computationally difficult measure $B(\rho)$ as

$$B(\rho) = \min \sum p_i b(\rho_i)$$

where the minimization is performed over all decompositions $\rho = \sum p_i \rho_i$ such that ρ_i is pure.

For the case of bipartite pure states, such entanglement monotones take on a particularly simple form. Let ρ_{AB} be a 2-qubit state and take $\rho_A = \mathrm{Tr}_B\, \rho_{AB}$. (We could equivalently use ρ_B.) The function $b(\rho_{AB})$ reduces to a unitary-invariant function $b'(\rho_A)$. Up to unitary invariance, ρ_A is completely characterized by its eigenvalues p and $1-p$. Thus, we can consider b' as a function of the eigenvalue p. For any entanglement monotone, this process yields a function that satisfies $b'(0) = b'(1) = 0$ and

$$b'(p_1\lambda_1 + p_2\lambda_2) > p_1 b'(\lambda_1) + p_2 b'(\lambda_2).$$

That is, b' is concave.

For 2-qubits, writing $b(\rho)$ in terms of an eigenvalue p of ρ_A gives

$$b'(p) \propto p(1-p).$$

2.6 Conclusion

In this chapter, we have shown that viewing the set of separable states as an orbitope provides substantial insight into the structure of entangled versus non-entangled states. Using the invariance of separable states under local unitary transformations, we constructed $E_{\min}$, the smallest-volume bounding ellipsoid of the separable states. While this object itself does not provide a particularly tight bound of the separable states, it can be used to construct an entanglement monotone which serves as a

measure of entanglement. In the multiqubit case, the ellipsoid dimensions give rise to a natural weighting of entanglement between different subsystems. Additionally, $E_{\min}$ provides insight into the geometrical structure of entanglement, demonstrating that the separable states are confined within a disk contained in the set of all valid states. In the field of algebraic geometry, orbitopes are still a topic of study, and this work demonstrates their potential use in quantum mechanics. An interesting extension of this work would be the determination of $E_{\max}$, or the largest-volume ellipsoid bounded by the separable states, which could in principle also be solved using the orbitope structure.

3 CLASSICAL SIMULATION OF QUANTUM NOISE

3.1 Introduction

When constrained to a physical system storing quantum information, entanglement is viewed as a resource. However, quantum information platforms are never fully isolated from their environments. As the system and environment interact, the system can become entangled with the environment. Even if the computational system begins in a pure state, tracing out the environment gives rise to a mixed state. Thus, the evolution of the system state is given by nonunitary evolution. Such a system is called open.

The notion of an open quantum system has received intense scrutiny in recent years, motivated initially by questions about the location and nature of the boundary (if any) between the quantum and classical worlds [13]. Further impetus has been given by the desire to minimize decoherence in quantum information processing [14, 15]. Open quantum systems have been conceived in two quite distinct ways: a system and bath considered as a single quantum entity with overall unitary dynamics, or a quantum system acted on by random classical forces. The first (system-bath or SB) approach is usually thought of as being more general since it includes the transformation of information and the idea that decoherence is connected to the entanglement of a system with its environment [16]. In the random classical (RC) force approach these effects are absent. Furthermore, in the question of the quantum-classical divide, it is often seen as important that the bath be macroscopic since this precludes the complete measurement of the bath degrees of freedom.

The SB approach is conveniently represented using Kraus operators. In this formalism, the system evolution is given by

$$\rho_S \to \sum_i E_i \rho E_i^\dagger$$

with the E_i satisfying

$$\sum E_i E_i^\dagger = I_S$$

where I_S is the identity operator. In the classical case, we impose the additional constraint that the Kraus operators are of the form $p_i U_i$ where each U_i is unitary.

It is very clear from the Kraus operator representation that the SB approach is more general than the RC one. However, this does not illuminate the precise role of entanglement in separating the SB and RC methods. In fact, it has been pointed out that SB models whose coupling is of dephasing type should always be able to be rewritten as classical models [17]. This is based on general results concerning existence of certain positive maps [18]. A specific example of a single qubit bath has been given [19]. Since SB entanglement is present in many dephasing models, this implies that this entanglement is not the decisive feature of SB models that distinguishes them from RC models.

In order to understand this particular aspect of the difference between quantum theory and classical physics, it would be useful to have a general explicit construction of a method to classically simulate quantum dephasing SB models. The possibility of such simulation of course does not imply that system-bath entanglement is not important for quantum decoherence, but it does imply that the distinction between quantum and classical noise is more subtle than has been previously recognized.

In this paper, we give the explicit construction of the classical model that corresponds to any given quantum dephasing in single qubit models and a restricted class of two-qubit models. As examples, we show explicitly how three paradigmatic system-macroscopic dephasing bath models can be simulated by subjecting the quantum 2-level system to a classical random force without ever needing the bath. We do this by describing completely the classical noise source that perfectly mimics the effect of entanglement of the qubit with the system. The three models are the popular spin-boson model, a specific central spin model, and the quantum impurity model. The last model is particularly interesting in this context since it has a "classical" and a "quantum" phase [20]. We also construct the classical simulations of certain 2-qubit models and show that pure depolarizing models can always be simulated classically

for an arbitrary number of qubits.

3.2 Classical simulation of quantum dephasing models

Quantum models

The class of quantum models considered here consists of a single qubit subject to dephasing by an arbitrary quantum system. Thus the total Hamiltonian of the open quantum system is

$$H = H_S\left[\sigma_i\right] + H_B\left[\lambda_i\right] + H_{SB}\left[\sigma_i, \lambda_i\right] \tag{3.1}$$

where $\sigma_{0,x,y,z}$ are the identity matrix and the Pauli matrices that act on the qubit and the matrices λ_j are some complete set of Hermitian operators for the bath, taken for simplicity to be finite-dimensional. $H_B\left[\lambda_i\right] + H_{SB}\left[\sigma_i, \lambda_i\right]$ are linear functions of the λ_i. λ_0 is proportional to the identity, and $\mathrm{Tr}_B\ \lambda_i = 0$ for $i > 0$. For an N-level bath the λ_i for $i > 0$ could be chosen as proportional to the $N^2 - 1$ generators of $SU\left(N\right)$ and $\lambda_0 = I/N$. Tr_B is the trace over bath variables. We shall normalize the λ_i by the condition that $\mathrm{Tr}_B\left[\lambda_i \lambda_j\right] = \delta_{ij}$ for $i, j > 0$. $H_B\left[\lambda_i\right]$ is the bath Hamiltonian. Infinite-dimensional baths can be treated by the same method at the cost of some additional notational complexity.

For a dephasing model, we take

$$\left[H_S, H_{SB}\right] = 0.$$

The total density matrix can be expanded as

$$\rho = \sum_{ij} N_{ij} \sigma_i \otimes \lambda_j \tag{3.2}$$

and we can invert this equation :

$$N_{ij} = \frac{1}{2} \operatorname{Tr} \left[\left(\sigma_i \otimes \lambda_j \right) \rho \right].$$

The reduced density matrix of the system is

$$\rho^S = \operatorname{Tr}_B \rho = \frac{1}{2} \sum_i n_i \sigma_i$$

and $n_i = (1, n_x, n_y, n_z)$ is the expanded Bloch vector of the system. For quantum noise we have

$$\rho(t) = U \rho(0) U^\dagger$$

with $U = \exp(-iHt)$ where we have set $\hbar = 1$. In terms of components this is

$$N_{ij}(t) = \frac{1}{2} \sum_{kl} \operatorname{Tr} \left[\left(\sigma_i \otimes \lambda_j \right) U \left(\sigma_k \otimes \lambda_l \right) U^\dagger \right] N_{kl}(0).$$

Let us write the initial ρ in a product form $\rho(0) = \rho^S(0) \otimes \rho^B(0)$, which in components says that $N_{ij}(0) = \frac{1}{2} n_i(0) m_j$, where

$$m_j = \operatorname{Tr}_B \lambda_i \rho^B(0).$$

Then the dynamics of the system can be rewritten as

$$N_{ij}(t) = \frac{1}{2} \sum_{kl} \operatorname{Tr} \left[\left(\sigma_i \otimes \lambda_j \right) U \left(\sigma_k \otimes \lambda_l(0) \right) U^\dagger \right] n_k(0) m_l$$

and the Bloch vector of the qubit at time t is given by

$$\begin{aligned} n_i(t) &= 2 N_{i0}(t) \\ &= \sum_{kl} \operatorname{Tr} \left[\left(\sigma_i \otimes \lambda_0 \right) U \left(\sigma_k \otimes \lambda_l(0) \right) U^\dagger \right] n_k(0) m_l \end{aligned}$$

Finally we have a linear relation between the initial and final expanded Bloch vectors:

$$n_i(t) = \sum_k T_{ik}^{(Q)} n_k(0)$$

where the quantum transfer matrix is given by

$$T_{ik}^{(Q)}(t) = \sum_l \mathrm{Tr}\left[(\sigma_i \otimes \lambda_0) U (\sigma_k \otimes \lambda_l) U^\dagger\right] m_l. \tag{3.3}$$

One should note that this represents a linear relation between the initial and final expanded Bloch vectors. However, if construed as a relation between the usual 3-dimensional Bloch vectors, it is an affine relation, since if $n_i(t=0) = (1,0,0,0)$, then the initial state has zero ordinary Bloch vector, but the final state has $n_i(t) = T_{i0}^{(Q)}$, which is not zero. Expanding the Bloch vector to four components is just a convenient way of including the affine part.

The whole dynamics of the qubit is contained in the matrix $T_{ik}^{(Q)}(t)$. Given an initial Hamiltonian, this matrix is uniquely defined.

Classical noise

A 2-level system acted on by dephasing classical noise has the 2×2 Hamiltonian

$$H_{Cl} = -\frac{1}{2} B \sigma_z + \frac{1}{2} h(t) \sigma_z. \tag{3.4}$$

$h(t)$ is a random classical (c-number) function of time that represents an external source of noise. To completely specify the model we need a probability functional $\mathcal{P}[h]$ on the noise histories. Then the system dynamics is given by

$$\begin{aligned} \rho^{(Cl)}(t) = \int \mathcal{D}[h(t')]\, \mathcal{P}[h(t')] \\ \times U_{Cl}[h(t')]\, \rho^{(Cl)}(0)\, U_{Cl}^\dagger[h(t')]. \end{aligned} \tag{3.5}$$

This is a functional integral over all real functions $h(t')$ defined on the interval $0 \leq t' \leq t$. Each $h(t')$ is assigned a probability $\mathcal{P}[h(t')]$ and

$$\int \mathcal{D}[h(t')]\,\mathcal{P}[h(t')] = 1.$$

Here the time-ordered exponential $U_{Cl}[h(t)] = \mathcal{T}\exp\left(-i\int_0^t H_{Cl}(t')\ dt'\right)$ is a 2×2 matrix, unlike $U_Q(t)$, which is infinite-dimensional. In the dephasing case two Hamiltonians taken at different times commute: $[H_{Cl}(t), H_{Cl}(t')] = 0$ and the time-ordering can be dropped. Note the simplicity of the classical problem relative to the quantum one.

We now follow the steps of the discussion of the quantum models with the appropriate modifications. Restating the results in terms of the 3×3 transfer matrix $T^{(Cl)}$, we have, in exact analogy to the section above,

$$\begin{aligned}
\rho^S &= \frac{1}{2}\sum_{i=0}^{3} n_i\sigma_i, \\
n_i &= \frac{1}{2}\operatorname{Tr}\sigma_i\rho^S \\
n_i(t) &= \sum_{j=0}^{3} T_{ij}^{(Cl)}(t)\, n_j(0)
\end{aligned}$$

where

$$\begin{aligned}
T_{ij}^{(Cl)}(t) =& \frac{1}{2}\int \mathcal{D}[h(t')]\,\mathcal{P}[h(t')]\times \\
& \operatorname{Tr}\left\{\sigma_i U_{Cl}[h(t')]\sigma_j U_{Cl}^{\dagger}[h(t')]\right\}
\end{aligned} \tag{3.6}$$

Note that $T_{i0}^{(Cl)} = \frac{1}{2}\operatorname{Tr}\sigma_i = \delta_{i0}$, so the classical model always gives a linear relation between initial and final ordinary Bloch vectors—there is no affine term.

Classical simulation of quantum models

To demonstrate the quantum-classical equivalence we need to prove the existence of a functional $\mathcal{P}[h(t)]$ such that $\rho_S^{(Cl)}(t) = \rho_S^{(Q)}(t)$, or, equivalently that $T_{ik}^{(Cl)}(t) =$

$T_{ik}^{(Q)}(t)$. For dephasing models we shall do more than this— we shall give the explicit construction of the classical model.

In the construction we shall need only the discrete version of Eq. (3.5), which is

$$\rho^{(Cl)}(t) = \sum_r p_r U_{Cl}^{(r)} \rho^{(Cl)}(t=0) U_{Cl}^{(r)\dagger},$$

where r labels the possible noise histories and $U_{Cl}^{(r)}$ is the evolution operator for that history. The positive numbers p_r satisfy $\sum_r p_r = 1$. The corresponding statement for the Bloch vector is

$$n_i(t) = \sum_{k,r} p_r O_{ik}^{(r)}(t) n_k(0), \tag{3.7}$$

and the $O_{ik}^{(r)}$ are orthogonal matrices for every r. Thus the problem of showing that a quantum noise model is actually classical reduces to the problem of showing that the matrix $T_{ik}^{(Q)}$ can be written as a convex combination of orthogonal matrices.

We shall consider the system-bath model of Eq. (3.1), choosing a total Hamiltonian

$$H = -\frac{1}{2} B\sigma_z + H_B[\lambda_i] + H_{SB}[\lambda_i]\sigma_z; \tag{3.8}$$

so that the qubit has no non-trivial dynamics and the noise is pure dephasing.

In this model σ_z is conserved, which implies that

$$T_{zz}^{(Q)} = 1\ ;\ T_{xz}^{(Q)} = T_{zx}^{(Q)} = T_{yz}^{(Q)} = T_{zy}^{(Q)} = 0.$$

We also have that $T_{00}^{(Q)} = 1$ and $T_{i0}^{(Q)} = T_{0i}^{(Q)} = 0$ for $i > 0$, so we only need to calculate $T_{xx}^{(Q)}, T_{yy}^{(Q)}, T_{xy}^{(Q)}$ and $T_{yx}^{(Q)}$.

First we note that the total evolution operator is

$$U_Q = \mathcal{T} \exp\left(-i \int_0^t H(t')\, dt'\right) = u(t) + v(t)\ \sigma_z,$$

where $u(t)$ and $v(t)$ are time-dependent bath operators and $\mathcal{T}$ denotes time-ordering.

Explicitly,

$$\begin{aligned} u(t) &= \frac{1}{2}\,\mathrm{Tr}_S\left[\mathcal{T}\exp\left(-i\int_0^t H(t')\,dt'\right)\right] \\ v(t) &= \frac{1}{2}\,\mathrm{Tr}_S\left[\sigma_z\mathcal{T}\exp\left(-i\int_0^t H(t')\,dt'\right)\right], \end{aligned} \tag{3.9}$$

where Tr_S is the trace over qubit variables. Note that these expressions do not depend in any way on having a finite-dimensional bath. Since $I = UU^\dagger$ we have

$$\begin{aligned} uu^\dagger + vv^\dagger &= I \\ uv^\dagger + vu^\dagger &= 0. \end{aligned}$$

Expressing $T^{(Q)}$ in terms of u and v we find

$$\begin{aligned} T^{(Q)}_{xx}(t) &= T^{(Q)}_{yy}(t) \qquad (3.10)\\ &= \mathrm{Tr}\left[\left(u^\dagger + v^\dagger\sigma_z\right)(\sigma_x\otimes\lambda_0)\left(u + v\sigma_z\right)\left(\sigma_x\otimes\rho^B(0)\right)\right] \\ &= 2\,\mathrm{Tr}_B\left[\left(u^\dagger u - v^\dagger v\right)\rho^B(0)\right] \\ T^{(Q)}_{xy}(t) &= -T^{(Q)}_{yx}(t) \qquad (3.11)\\ &= \mathrm{Tr}_B\left[\left(u^\dagger + v^\dagger\sigma_z\right)(\sigma_x\otimes\lambda_0)\left(u + v\sigma_z\right)\left(\sigma_y\otimes\rho^B(0)\right)\right] \\ &= \mathrm{Tr}_B\left[\left(-2iu^\dagger v + 2iv^\dagger u\right)\rho^B(0)\right], \end{aligned}$$

and defining $c = T^{(Q)}_{xx} = T^{(Q)}_{yy}$ and $s = -T^{(Q)}_{xy} = T^{(Q)}_{yx}$, the matrix $T^{(Q)}$ has the form

$$T^{(Q)} = \begin{pmatrix} 1 & 0 & 0 & 0 \\ 0 & c & -s & 0 \\ 0 & s & c & 0 \\ 0 & 0 & 0 & 1 \end{pmatrix}.$$

with positivity implying that $c^2 + s^2 = r^2 \leq 1$. The submatrix $T^{(Q)}_{ij}$ with $i, j = x, y$ is proportional to an orthogonal 2×2 matrix. All effects of the bath on the system are summarized by the quantities $c(t)$ and $s(t)$.

The task is now to construct the equivalent classical model. In two dimensions,

an orthogonal matrix M is characterized by a single unit vector $(\cos\theta, \sin\theta)$, so a convex sum of orthogonal matrices is of the form

$$\sum_i p_i M_i = \begin{pmatrix} \sum_i p_i \cos\theta_i & -\sum_i p_i \sin\theta_i \\ \sum_i p_i \sin\theta_i & \sum_i p_i \cos\theta_i \end{pmatrix},$$

with $p_i > 0$ and $\sum_i p_i = 1$. This matrix is proportional to the $i, j = x, y$ submatrix of $T_{ij}^{(Q)}$.

We first write the vector (c, s) as the convex sum of unit vectors:

$$\begin{pmatrix} c \\ s \end{pmatrix} = \frac{1}{2}\begin{pmatrix} c + \beta s \\ s - \beta c \end{pmatrix} + \frac{1}{2}\begin{pmatrix} c - \beta s \\ s + \beta c \end{pmatrix}$$

where

$$r^2 = c^2 + s^2 = \left[T_{xx}^{(Q)}\right]^2 + \left[T_{xy}^{(Q)}\right]^2 \; ; \; \beta = \frac{\sqrt{1 - r^2}}{r} \tag{3.12}$$

(It is interesting to note that this decomposition of the vector (c, s) is not unique.) Then the classical evolution submatrix is written as

$$T^{(Cl)} = \frac{1}{2}\begin{pmatrix} \cos\Phi_1 & \sin\Phi_1 \\ -\sin\Phi_1 & \cos\Phi_1 \end{pmatrix} + \frac{1}{2}\begin{pmatrix} \cos\Phi_2 & \sin\Phi_2 \\ -\sin\Phi_2 & \cos\Phi_2 \end{pmatrix}.$$

$T^{(Cl)}$ is the convex sum of rotations through the two angles

$$\begin{aligned} \Phi_1(t) &= \tan^{-1}\left(\frac{s - \beta c}{c + \beta s}\right) \\ &\text{and} \\ \Phi_2(t) &= \tan^{-1}\left(\frac{s + \beta c}{c - \beta s}\right). \end{aligned} \tag{3.13}$$

Hence, by comparison to Eq. (3.7), it defines a classical model. Define the fields

$h_1(t)$ and $h_2(t)$ by

$$\begin{aligned} h_1 =& \frac{\partial \Phi_1}{\partial t} + B \\ & \text{and} \\ h_2 =& \frac{\partial \Phi_2}{\partial t} + B. \end{aligned} \tag{3.14}$$

Then the equivalent classical model is given by

$$H_{Cl} = -\frac{1}{2} B \sigma_z + \frac{1}{2} h(t) \sigma_z$$

and the probability distribution for h is: $h(t) = h_1(t)$ with probability $1/2$ and $h(t) = h_2(t)$ with probability $1/2$. More formally, $\mathcal{P}[h(t)] = (1/2)\delta[h - h_1] + (1/2)\delta[h - h_2]$. Writing $\Phi_i(t) = \int_0^t (-B + h_i(t'))\, dt'$ and following Eq. (3.6) we find

$$\begin{aligned} T_{ij}^{(Cl)} =& \frac{1}{4} \operatorname{Tr}\left[\sigma_i e^{\frac{i}{2}\sigma_z \Phi_1(t)} \sigma_j e^{-\frac{i}{2}\sigma_z \Phi_1(t)}\right] \\ & + \frac{1}{4} \operatorname{Tr}\left[\sigma_i e^{\frac{i}{2}\sigma_z \Phi_2(t)} \sigma_j e^{-\frac{i}{2}\sigma_z \Phi_2(t)}\right] \end{aligned}$$

The contents of this section can be summarized by the following theorem and *constructive* proof.

Theorem 3.1. *The dynamics of the open quantum system given by Eq. (3.8) can be simulated by the classical noise model given by Eq. (3.4) with $h(t)$ given by Eqs. 3.14: the density matrix of the qubit is the same for the two models at all times.*

Proof. The quantum Hamiltonian H of Eq. (3.8) determines the noise functions $u(t)$ and $v(t)$ in Eqs. (3.9) and hence the matrix $T^{(Q)}$ in Eqs. (3.10) and (3.11) uniquely. The classical fields $h_1(t)$ and $h_2(t)$ are given explicitly in terms of the matrix elements of $T^{(Q)}$ by Eqs. (3.12) through (3.14). $h_1(t)$ and $h_2(t)$ in turn define the classical Hamiltonian H_{Cl} and noise probability functional $\mathcal{P}$ given in Eqs. (3.4) and (3.5). The evolution of the qubit density matrix according to H_Q with the usual partial trace is precisely the same as the qubit evolution according to the classical Hamiltonian H_{Cl} with the averaging over noise histories. □

3.3 Classical simulation of dephasing models

Spin-boson model

The spin-boson Hamiltonian is

$$H_{SB} = -\frac{1}{2}B\sigma_z + \sigma_z \sum_k \left(g_k b_k^\dagger + g_k^* b_k \right) + \sum_k \omega_k b_k^\dagger b_k.$$

The initial density matrix is $\rho(t=0) = \rho_S(t=0) \otimes \rho_B(t=0)$, where $\rho_S(t=0)$ is the initial state of the 2-level system and $\rho_S(t=0)$ is the thermal state of the bath at temperature $1/\beta$. We are interested in the case of a macroscopic bath, and it is then conventional to define the coupling function

$$J(\omega) = 4 \sum_k \delta(\omega - \omega_k) |g_k|^2 .$$

Using $U_Q(t) = \exp(-iH_Q t)$, the system dynamics is given by

$$\rho_S^{(Q)}(t) = \mathrm{Tr}_B \, U_Q(t) \, \rho(t=0) \, U_Q^\dagger(t) .$$

The initially unentangled system and bath are entangled by $U_Q(t)$. This model has been well-studied and is exactly solvable [21], with the result that the off-diagonal elements of $\rho_S(t)$ are proportional to $e^{\Gamma(t)}$, where

$$\Gamma(t) = -\int_0^\infty d\omega \; J(\omega) \coth(\beta\omega/2) (1 - \cos\omega t) / \omega^2 < 0.$$

More explicitly,

$$\begin{aligned}\rho^{(Q)} =& \begin{pmatrix} \rho_{00} & \rho_{01}e^{\Gamma(t)+iBt} \\ \rho_{10}e^{\Gamma(t)-iBt} & \rho_{11} \end{pmatrix} \\ =& \frac{\rho_{00}+\rho_{11}}{2}\sigma_0 + \frac{\rho_{00}-\rho_{11}}{2}\sigma_z \\ &+ \frac{1}{2}e^{\Gamma(t)}\left(\rho_{01}e^{iBt}+\rho_{10}e^{-iBt}\right)\sigma_x \\ &+ \frac{1}{2}e^{\Gamma(t)}\left(\rho_{10}e^{-iBt}-\rho_{01}e^{iBt}\right)\sigma_y.\end{aligned}$$

ρ_{ij} are the (time-independent) initial values for the elements of ρ. In terms of the Bloch vector we have

$$\begin{aligned}n_x(t) &= e^{\Gamma(t)}\left(n_x(0)\cos Bt + n_y(0)\sin Bt\right) \\ n_y(t) &= e^{\Gamma(t)}\left(-n_x(0)\sin Bt + n_y(0)\cos Bt\right)\end{aligned}$$

We are free to consider the polarization vector along the z direction by change of basis and we can also begin with a pure state since total evolution is simply proportional to the initial polarization vector. Written in terms of elements of $T^{(Q)}$,

$$\begin{aligned}c_{sb} &= e^{\Gamma(t)}\cos Bt \\ s_{sb} &= -e^{\Gamma(t)}\sin Bt \\ \beta_{sb} &= \frac{\sqrt{1-e^{2\Gamma(t)}}}{e^{\Gamma(t)}}.\end{aligned}$$

According to the prescription in the previous section, therefore,

$$H_{Cl}^{(sb)} = -\frac{1}{2}B\sigma_z + \frac{1}{2}h^{(sb)}(t)\,\sigma_z$$

and the noise source $h^{(sb)}(t)$ is

$$\begin{aligned} h_1^{(sb)}(t) &= \frac{\partial}{\partial t}\tan^{-1}\left(\frac{s_{sb}-\beta_{sb}c_{sb}}{c_{sb}+\beta_{sb}s_{sb}}\right)+B\ ;\ p_1=\frac{1}{2} \\ h_2^{(sb)}(t) &= \frac{\partial}{\partial t}\tan^{-1}\left(\frac{s_{sb}+\beta_{sb}c_{sb}}{c_{sb}-\beta_{sb}s_{sb}}\right)+B\ ;\ p_2=\frac{1}{2} \end{aligned} \tag{3.15}$$

where p_i is the probability of h_i.

Eq. 3.15 gives the result for a general coupling function $J(\omega)$. A common choice for J is the ohmic bath: $J(\omega)=A\omega e^{-\omega/\Omega}$, important in quantum optics. In this case there is [21] the exact result

$$\Gamma(t) \propto -\frac{1}{2}\ln\left(1+\Omega^2t^2\right)-\ln\left(\frac{\sinh(t/\tau)}{t/\tau}\right).$$

where Ω is the cutoff frequency and $\tau=\frac{1}{\pi T}$ is the thermal correlation time where we have taken $k_B=1$. This expression for $\Gamma(t)$ allows an exact calculation of $h_1(t)$ and $h_2(t)$ up to an overall scale factor. The results of this calculation are plotted in Fig. 3.1 for the case $\Omega\tau=20$ where we have taken the overall scale factor to be one.

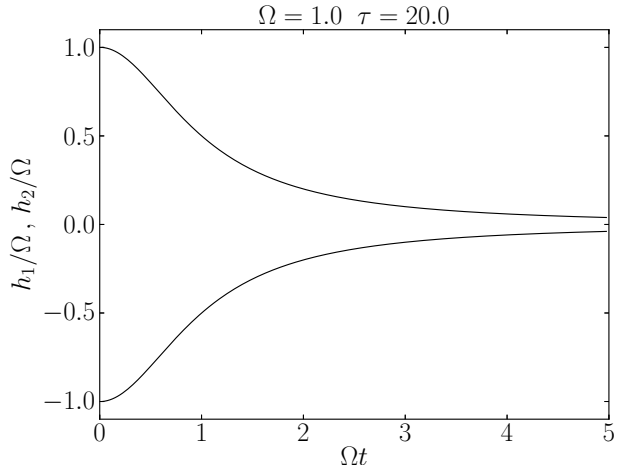

Figure 3.1: Fields $h_1(t)$ and $h_2(t)$ for the spin-boson model.

The classical fields have a complicated form, with an initial quadratic decay

crossing over to exponential at longer times. The behavior for $t \gg \tau$ is due to thermal decay while the behavior for $t \ll \tau$ is determined by the cutoff Ω and is due to fluctuations of the field [21].

Central spin model

The central spin Hamiltonian describes a qubit coupled to a bath of nuclear spins. In the case of free induction decay, the Hamiltonian is

$$H_{CS} = -\frac{1}{2}B\sigma_z + H_{int} + H_{hf}$$

where

$$H_{int} = \sum_i \omega_i J_i^z + \sum_{i \neq j} b_{ij} \left(J_i^+ J_j^- - 2 J_i^z J_j^z \right)$$

and

$$H_{hf} = \sigma_z \left(\frac{1}{2} \sum_i A_i J_i^z + \sum_{i \neq j} \frac{A_i A_j}{4B} J_i^+ J_j^- \right).$$

ω_i are the nuclear Zeeman splittings, b_{ij} contain the dipolar interaction, and A_i are the hyperfine couplings. We assume that the initial state is a product state of the qubit and the equilibrium bath state. For realistic conditions on ω_i, b_{ij}, and A_i, the qubit dynamics can be calculated approximately at experimentally relevant time scales [22–24]. The off-diagonal component of the qubit density matrix is given by $\rho_{10}(t) = \rho_{10}(0) D_{cs}(t)$ where

$$D_{cs}(t) = \frac{e^{i \arctan(\alpha t) - iBt}}{\sqrt{1 + \alpha^2 t^2}}$$

where α is a complicated function of the parameters of the model. The explicit dependence is found in [22] and α determines the relevant time scales since the model is valid only for $\alpha t \ll 1$. In reference [22], $1/\alpha \approx 20\,\mu$s for GaAs dot.

The qubit gains an additional phase from the bath interaction. In terms of $T^{(Q)}$,

we have

$$
\begin{aligned}
c_{cs} &= \frac{1}{\sqrt{1+\alpha^2 t^2}} \cos\left(\arctan\left(\alpha t\right) - Bt\right) \\
s_{cs} &= \frac{1}{\sqrt{1+\alpha^2 t^2}} \sin\left(\arctan\left(\alpha t\right) - Bt\right) \\
\beta_{cs} &= \frac{\alpha t}{\sqrt{1+\alpha^2 t^2}}.
\end{aligned}
$$

Then we can write

$$
\begin{aligned}
\Phi_1 &= -Bt + \arctan\left(\alpha t\right) + \arcsin\left(\frac{\alpha t}{\sqrt{1+\alpha^2 t^2}}\right) \\
\Phi_2 &= -Bt + \arctan\left(\alpha t\right) - \arcsin\left(\frac{\alpha t}{\sqrt{1+\alpha^2 t^2}}\right)
\end{aligned}
$$

Noting that $\arctan\left(\alpha t\right) = \arcsin\left(\frac{\alpha t}{\sqrt{1+\alpha^2 t^2}}\right)$ and applying Eqs. (3.14) we get

$$
\begin{aligned}
h_1^{(cs)}\left(t\right) =& \frac{2\alpha}{1+\alpha^2 t^2} \\
& \text{and} \\
h_2^{(cs)}\left(t\right) =& 0.
\end{aligned}
$$

This model shows a Lorentzian fall-off of one of the two possible fields but the other one vanishes. Unlike the spin-boson model, these fields have a non-zero time average which indicates that the central spin noise induces an additional relative phase ϕ between the two system states. Furthermore, if we write the decoherence function as $re^{i\phi}$, for $r, \phi \in \mathbb{R}$ so that $\rho_{10}(t) = \left(\rho_{10}(0)e^{-iBt}\right)\left(r(t)e^{i\phi(t)}\right)$, then the central spin model gives a simple relation between r and ϕ. Namely, $r = \cos\phi$ for all values of t.

Quantum impurity model

The quantum impurity Hamiltonian is

$$H_{QI} = -\frac{1}{2}B\sigma_z + \frac{1}{2}v\left(d^\dagger d\right)\sigma_z + H_B$$

where

$$H_B = \epsilon_0 d^\dagger d + \sum_k \left(t_k c_k^\dagger d + \text{H.c.}\right) + \sum_k \epsilon_k c_k^\dagger c_k.$$

$c_k^\dagger$ creates a reservoir electron and $d^\dagger$ creates an impurity electron. v represents the qubit-impurity coupling strength and t_k are the tunneling amplitudes between the impurity and level k. Define the tunneling rate $\gamma = 2\pi \sum_k |t_k|^2 \delta(\epsilon_k - \epsilon_0)$. Assuming an initial product state and an equilibrium bath, this model can be solved via numerically exact techniques [25]. The off-diagonal components of the qubit density matrix satisfy

$$\rho_{10}(t) = \rho_{10}(0)\, e^{-iBt} D_{qi}(t).$$

Using the numerical methods outlined in [25], we compute $D(t) = r(t)e^{i\phi(t)}$ for $r(t) > 0$. Applying the method outlined earlier yields

$$\Phi_i = -Bt + \phi(t) \pm \cos^{-1}(r(t))$$

and the classical noise source $h^{(qi)}(t)$ can be calculated using Eqs. (3.14). Numerical results are shown in Fig. 3.2.

This model is of particular interest because it shows a "classical" phase for $v \ll \gamma$ and a "quantum" phase for $v \gg \gamma$ with a crossover region in between. The quantum phase is characterized by oscillation in the coherence measures such as the visibility. These oscillations are clearly caused by the oscillations in the noise fields as shown in Fig. 3.2. There is, however, nothing quantum about the fields at any value of v: they are classical noise sources.

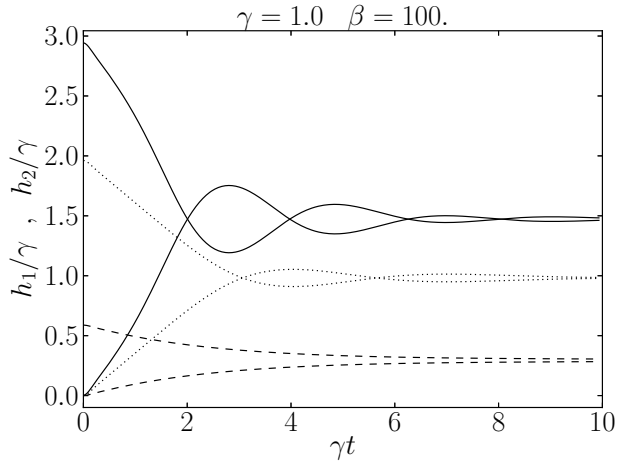

Figure 3.2: Fields $h_1(t)$ and $h_2(t)$ for the quantum impurity model. The solid line shows coupling $v = 3$ (quantum phase). The dotted line shows $v = 2$ (crossover). The dashed line shows $v = 0.6$ (classical phase). Note the oscillatory behavior of the stronger coupling, indicative of coherence oscillation.

3.4 Two-qubit dephasing

We consider a classical two-qubit dephasing model with a Hamiltonian of the form

$$H = H_S + H_B + H_{SB}$$

such that all diagonal two-qubit Pauli operators commute with the total Hamiltonian. That is,

$$[H, \sigma_i \otimes \sigma_j] = 0$$

for $i, j \in \{0, 3\}$. Note that these diagonal Pauli operators also commute with each other. We assume that the system and bath are initially in a product state so that the two-qubit system is in the initial state ρ_S. The diagonal elements of the two-qubit reduced density matrix will remain constant under time evolution. For a classical noise source to simulate the system-bath Hamiltonian and preserve the diagonal elements, each noise source must commute with each diagonal Pauli. Thus, the time evolution of the density matrix is given by $\rho_{ij}(t) = r_{ij}(t)\rho_{ij}(0)$ for $r_{ij}(t) = r_{ji}(t)^*$,

$|r_{ij}(t)| \leq 1$, and $r_{ii}(t) = r_{ij}(0) = 1$.

Consider a classical noise source H_α with probability distribution $p(\alpha)$ for $\alpha \in \mathbb{R}$. The corresponding evolution of the two-qubit density matrix is given by

$$\rho(t) = \int_{-\infty}^{\infty} p(\alpha) U_\alpha(t) \rho(0) U_\alpha^\dagger(t) d\alpha.$$

In order to preserve the diagonal entries, we must have that each H_α is a linear combination of diagonal two-qubit Paulis. Note that the diagonal Paulis span the entire set of Hermitian diagonal matrices so we can consider each H_α as a diagonal matrix with diagonal entries $\alpha d_i^\alpha(t)$ where we have chosen to scale each H_α by the parameter α. Then, time evolution is given by diagonal unitary operators U_α with diagonal entries $\exp\left(-i\alpha\theta_i^\alpha(t)\right)$ for

$$\theta_i^\alpha(t) = \int_0^t d_i^\alpha(t') dt'.$$

Then the action $U_\alpha \rho U_\alpha^\dagger$ gives

$$\rho_{ij} \to e^{-i\alpha\gamma_{ij}^\alpha(t)} \rho_{ij}$$

where $\gamma_{ij}^\alpha(t) = \theta_i^\alpha(t) - \theta_j^\alpha(t)$. We now make a simplifying assumption that H_α is simply proportional to α so that $\gamma_{ij}^\alpha(t) = \gamma_{ij}(t)$. Applying this result and averaging the result over the probability distribution gives

$$\begin{aligned} \rho_{ij}(t) =& \int_{-\infty}^{\infty} p(\alpha) \rho_{ij}(0) e^{-i\alpha\gamma_{ij}(t)} d\alpha \\ =& \rho_{ij}(0) \tilde{p}\left(\gamma_{ij}(t)\right) \end{aligned} \tag{3.16}$$

where $\tilde{p}(t) = \int_{-\infty}^{\infty} p(\alpha) e^{-i\alpha t} d\alpha$. That is, for the model specified above,

$$r_{ij}(t) = \tilde{p}(\gamma_{ij}(t)). \tag{3.17}$$

This model gives a highly restrictive set conditions of $r_{ij}(t)$. However, note that we

can again average over a variety of such models to obtain more complicated behavior.

3.5 n-dimensional depolarization

Given a quantum system in N dimensions with initial density matrix ρ_0, the depolarization channel is given by

$$\rho(t) = (1 - p(t))\rho_0 + p(t)\left(\frac{1}{N}\right) I$$

where $p(t) \in [0, 1]$ for all t and $p(0) = 0$.

We now present a classical model for depolarization in arbitrary dimension. Consider the unitary group $SU(N)$. Each time-independent $U \in SU(N)$ can be expanded in terms of its eigenvectors $|j\rangle$ as

$$U = \sum_j e^{-id_j} |j\rangle \langle j|$$

where the eigenvalues of d_j are all in $[-\pi, \pi]$. For a fixed U, define H_U as

$$H_U = \sum_j d_j |j\rangle \langle j|$$

so that

$$U = e^{-iH_u t}\big|_{t=1}$$

Note that each H_U can be expanded as

$$H_U = \sum_r h_r \lambda_r$$

where h_r are real and λ_r are the generators of $SU(N)$. Then consider the Hamiltonian defined by the set $\{H_U\}$ with the probability distribution equal to the uniform

distribution over the unitary group. For convenience, choose

$$\int_{SU(N)} dU = 1$$

where the integral is taken with respect to the Haar measure. Time evolution is then given by

$$\rho(t) = \int_{SU(N)} e^{-iH_U t}\rho(0)e^{iH_U t}dU. \tag{3.18}$$

We need to show that this time evolution is purely depolarizing: the polarization vector remains parallel to the initial polarization vector at all values of t and $\rho(1)$ is proportional to the identity giving the totally mixed state. Let ρ_0 be given by polarization vector v so that

$$\rho(0) = \frac{1}{N}I + \sum_r v_r\lambda_r.$$

Then consider the unitary operator

$$V = \exp\left(i\alpha\sum_r v_r\lambda_r\right).$$

where α is an arbitrary non-zero real number. It is clear that

$$V\rho_0 V^\dagger = \rho_0$$

and we can write that

$$\rho(t) = \int_{SU(N)} e^{-iH_U t}V\rho_0 V^\dagger e^{iH_U t}dU$$

from which we can easily obtain

$$V^\dagger\rho(t)V = \int_{SU(N)} V^\dagger e^{-iH_U t}V\rho_0 V^\dagger e^{iH_U t}V dU.$$

Since the above integral runs over the entire unitary group $SU(N)$, conjugation by V simply amounts to a reparameterization of the integral. Thus, we can write

$$V^\dagger \rho(t) V = \int_{SU(N)} e^{-iH_U t} \rho_0 e^{iH_U t} dU = \rho(t). \tag{3.19}$$

Hence, any rotation leaving the initial polarization vector fixed must also leave $\rho(t)$ fixed, the polarization vector of $\rho(t)$ must be parallel to that of ρ_0.

Now, consider the case $t = 1$. From our initial definition of H_U, we see that

$$\rho(1) = \int_{SU(N)} U \rho_0 U^\dagger dU.$$

Further consider an arbitrary unitary operator W. Then conjugation gives

$$\begin{aligned} W\rho(1)W^\dagger &= \int_{SU(N)} WU\rho_0 U^\dagger W^\dagger dU \\ &= \int_{SU(N)} U\rho_0 U^\dagger dU \end{aligned}$$

since if U runs over the entire unitary group than so does WU. Thus, we see that

$$W\rho(1)W^\dagger = \rho(1).$$

Since this holds for arbitrary unitary operator W, we must have that $\rho(1)$ is proportional to the identity. Thus, $\rho(1)$ is the totally mixed state and we see that the model presented is indeed a depolarizing channel.

Single qubit case

For the single qubit case, the depolarizing behavior can be evaluated explicitly. Without loss of generality, assume that the qubit state is specified by

$$\rho(0) = \frac{1}{2}\left(I + \sigma_z\right).$$

Then

$$\rho(t) = \frac{1}{2}\left(I + n_z(t)\sigma_z\right).$$

Then the integral in Eq. 3.18 becomes

$$I/2 + \frac{1}{2}\int_{SU(2)} U(t)ZU(t)^\dagger.$$

Note that we can write any element of $SU(2)$ as

$$U = \begin{pmatrix} a & -\bar{b} \\ b & \bar{a} \end{pmatrix}$$

where $a^2 + b^2 = 1$. Writing $a = x + iy$ and $b = w + iz$ it is clear that $SU(2)$ is the manifold S^3. Furthermore, the Haar measure on $SU(2)$ is simply the standard Euclidean measure on the unit 3-sphere, although we will use a different parametrization. Any element U in $SU(2)$ has eigenvalues $e^{\pm i\lambda}$ and we can write a normalized eigenvector as

$$|+\rangle = \cos\frac{\theta}{2}|0\rangle + e^{i\phi}\sin\frac{\theta}{2}|1\rangle.$$

Thus, we can write any element in $SU(2)$ as

$$U = e^{i\lambda}\left(|+\rangle\langle+|\right) + e^{-i\lambda}\left(I - |+\rangle\langle+|\right).$$

Writing $\cos\frac{\theta}{2} = c$ and $\sin\frac{\theta}{2} = s$ we get

$$U = \left(e^{i\lambda} - e^{-i\lambda}\right)\left(|+\rangle\langle+|\right) + e^{-i\lambda}I = 2i\sin\lambda\begin{pmatrix} c^2 & e^{-i\phi}cs \\ e^{i\phi}cs & s^2 \end{pmatrix} + \begin{pmatrix} e^{-i\lambda} & 0 \\ 0 & e^{-i\lambda} \end{pmatrix}.$$

To determine how to embed this into the 3-sphere, we only need to look at the 00 and 01 components. This gives

$$U_{00} = 2i\sin\lambda c^2 + \cos\lambda - i\sin\lambda = \cos\lambda + i\sin\lambda\left(2c^2 - 1\right) = \cos\lambda + i\sin\lambda\cos\theta$$

and

$$U_{01} = 2i \sin\lambda e^{-i\phi} cs = \sin\lambda \sin\theta \sin\phi + i \sin\lambda \sin\theta \cos\phi.$$

Now we can look at the four components of the 3-sphere and we see that this parametrization is just the generalized spherical coordinates. Then we can write the properly normalized measure

$$dU = \frac{1}{2\pi^2} \sin^2\lambda \sin\theta d\lambda d\theta d\phi.$$

To give U the correct time dependence for depolarization, simply replace λ with λt in each U, but leave the measure $\sin^2\lambda d\lambda$ unchanged. Calculating $U\sigma_z U^\dagger$ gives the ρ_{00} component $\cos^2\theta + \cos(2\lambda t)\sin^2\theta$. Then we get

$$n_z(t) = \frac{1}{2\pi^2} \int_0^{2\pi} \int_0^{\pi} \int_0^{\pi} \left(\cos^2\theta + \cos(2\lambda t)\sin^2\theta\right) \sin^2\lambda \sin\theta d\lambda d\theta d\phi.$$

Evaluating this integral gives

$$n_z(t) = \frac{1}{3} + \frac{\sin(2\pi t)}{3\pi t(1-t^2)}.$$

This expression indeed satisfies $n_z(0) = 1$ and $n_z(1) = 0$. Somewhat surprisingly, this function has a root near $t = 0.77$ and has a limiting value of $1/3$ as $t \to \infty$. Because of the root, proper depolarization behavior ends before $t = 1$, however a simple reparametrization of time allows for more general depolarizing behavior. The graph of $n_z(t)$ is shown in Fig. 3.3.

3.6 Conclusion

By comparing quantum noise models to classical noise models, we have shown that classical noise models are capable of recreating a broad set of noise features, including some models that realize behavior that had previously been viewed as distinctly quantum.

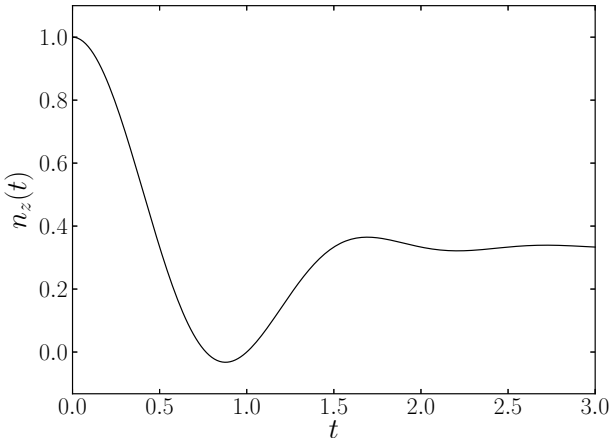

Figure 3.3: The magnitude of the single-qubit Bloch vector as a function of time for classical depolarization. Note that proper depolarization ends at the first root ($t \approx 0.77$).

For a single qubit, we explicitly construct classical noise terms that can simulate arbitrary dephasing noise. For two qubits, we demonstrate how certain dephasing models can be constructed, and show how the technique can be used to build more complicated models. Finally, we showed that depolarization can be realized classically for quantum systems of arbitrary dimension.

In a practical sense, these results can be used to tune noise models for classical simulations of quantum systems. Philosophically, it is interesting to note that dephasing noise is easily realized classically,

4 MEASUREMENT-FREE ERROR CORRECTION

4.1 Introduction

Due to the inherent fragility of quantum systems, quantum computation was not widely seen as a realistic possibility until 1995 when Shor demonstrated the possibility of quantum error correction codes [26]. In the subsequent year, the theory of quantum error correction was expanded [27–32] and expanded into the more general notion of fault tolerant quantum computing [33–36]. Broadly, the results concluded that scalable quantum computation is possible if error rates are sufficiently low. The general technique is to use multiple entangled physical qubits to represent a single logical qubit in a manner that allows local errors to be corrected.

Since the initial flurry of work in 1995-96, error correction has continued to advance in both theoretical and experimental settings. On the theoretical side, general goals have been to improve error thresholds by using better codes and optimizing architecture. Kitaev's topological codes, introduced in 1997, generated notable optimism [37–39]. Experimentally, small scale error correction protocols have been demonstrated in both superconducting and trapped ion qubits [40–43]. A fully protected logical qubit has not yet been demonstrated, although this goal is currently being pursued in several physical systems [44–47].

We are primarily motivated here by qubits realized as an array of neutral atoms held in optical or magnetic traps [48, 49]. The quantum information is stored in atomic hyperfine clock states. This system has several attractive features: each natural qubit is identical, clock states exhibit long coherence times measured in seconds, and state preparation and measurement can be performed on msec timescales using well-developed techniques of optical pumping and detection of resonance fluorescence [50, 51]. Arrays of individually addressable neutral atom qubits have been demonstrated in 1D [52, 53], 2D [54–57], and 3D [58]. Qubit numbers of order 100 have been demonstrated in 2D and 3D and in principle these numbers could be extended to several thousands using available technology. Lastly, the available gate set is universal, based on microwave and laser light for single qubit rotations together with Rydberg

state mediated interactions for two-qubit, and multi-qubit, entangling gates [49].

Achieving logical protection requires an error correction procedure compatible with available operations. Standard error correction protocols rely on performing frequent syndrome measurements [14, 38]. This turns out not to be well suited for neutral atom implementations for two reasons. First, the time needed for state measurements is currently several orders of magnitude longer than for gate operations. Second, it is difficult to measure a single atomic qubit in an array without scattered light corrupting the state of nearby qubits, although a number of possible solutions to this problem are under study [59].

These challenges motivate the consideration of coherent, or measurement-free, error correction methods [60–63]. Like standard measurement-based error correction [44–47], techniques for measurement-free error correction are based on stabilizer codes. However, there has been strong skepticism that measurement-free error correction can produce error thresholds close to those of measurement-based [27, 29, 34], though Paz-Silva *et al.* did achieve a measurement-free threshold only about one order of magnitude worse than measurement-based [61]. We improve this result by nearly 2 orders of magnitude by taking advantage of the resources available to neutral atoms, in combination with a novel syndrome extraction technique.

Measurement-free error correction is particularly attractive for neutral atom and trapped ion approaches that rely on light scattering for entropy removal. As part of an error correction cycle, entropy in the data qubits is transferred to fresh ancilla qubits, and is subsequently removed by resetting the ancillas. Although an ancilla reset requires optical pumping and light scattering, the number of scattered photons is typically 1–2 orders of magnitude less than would be needed for state measurement in measurement-based error correction.

Measurement-free error correction can additionally benefit from an additional resource of neutral atom systems, since the computational capabilities include native Toffoli and C_kNOT gates. These C_kNOTs can potentially achieve fidelities as high as 90% for $k \sim 35$, while for smaller k the fidelities of the native gates are expected to beat fidelities of the decompositions into 1- and 2-qubit gates [64, 65]. Similarly, Rydberg interactions allow for parallel CNOT gates in which a single control qubit

targets multiple qubits simultaneously, improving the time required for syndrome extraction. Native Toffoli gates have also been demonstrated using trapped ion [66] and superconducting qubits [67]; thus the techniques presented here could potentially be adapted to other platforms.

Using numerical simulation, we estimated threshold error rates using neutral atom resources for three well known error correction schemes: the bit-flip code, the Bacon-Shor code, and the Steane code. For these codes, we found threshold error rates of $\sim 10^{-2}$–10^{-4} for realistic conditions, demonstrating that measurement-free error correction can achieve thresholds that are comparable to those of measurement-based techniques.

The structure of the chapter is organized as follows. We begin with a review of stabilizer codes and measurement-based error correction procedures. Then we discuss how these techniques are adapted for neutral atoms, including the novel method of using an extended set of stabilizers, which is also applicable to measurement-based error correction. In the following portion, we provide details on the simulation and discuss the results.

4.2 Stabilizer codes

Here, we will think of errors as unitary operators E that act nontrivially on w qubits, where w is called the weight of the operator. A general operator on w qubits can be expanded in terms of the Pauli operators on those qubits, and it is sufficient to consider Pauli operators, which we will discuss in further detail later.

Basics of stabilizer codes

A $[n, k, d]$ error correction code uses n physical qubits to encode k logical qubits. The distance d of the code is the weight of the smallest error that cannot be detected. For the three codes discussed here, $k = 1$.

An $[n, 1, d]$ code is determined by a set of $n-1$ stabilizers, $\{S_i\}$, logical operators Z_L and X_L, and logical states $|0\rangle_L$ and $|1\rangle_L$. All operators S_i, Z_L, and X_L are taken

to be Pauli operators. For a linear combination of the logical states $|\psi\rangle$, the following conditions must be satisfied:

1. $[S_i, S_j] = [S_i, Z_L] = [S_i, X_L] = 0$
2. $\{X_L, Z_L\} = 0$
3. $S_i |\psi\rangle = |\psi\rangle$.

Furthermore, when restricted to the logical states, Z_L and X_L act as the standard Z and X single-qubit operators. The final condition justifies the name stabilizers, since these operators stabilize the logical subspace. Note that formally these are actually stabilizer generators, and the full stabilizer subgroup is composed of all products of the generators.

Let E be a Pauli operator representing an error on the data qubits. In order to detect this error, at least one stabilizer S_i must satisfy

$$[E, S_i] \neq 0.$$

Note that since E and S_i are both Paulis, this implies that $\{E, S_i\} = 1$. Now the distance d of the code is the lowest-weight operator E that commutes with all stabilizers, but that acts nontrivially on the logical subspace.

To see how we use these stabilizers to correct errors, it is helpful to note that the simultaneous eigenstates of Z_L and $\{S_i\}$ form a basis. Thus, the entire space is spanned by states of the form

$$|\phi\rangle = |\lambda_Z, \lambda_1, \ldots, \lambda_{n-1}\rangle$$

where the λ are given by $Z_L |\phi\rangle = \lambda_Z |\phi\rangle$ and $S_i |\phi\rangle = \lambda_i |\phi\rangle$ with $\lambda = \pm 1$. Any state in the logical subspace can be written

$$|\psi\rangle = |\psi_L\rangle |1, 1, \ldots, 1\rangle .$$

After an error E, the state $E|\psi\rangle$ will have eigenvalues $\lambda_i = -1$ if E and S_i anticommute. The set of stabilizer eigenvalues $\{\lambda_i\}$ is called the error syndrome, or simply the syndrome.

Measurement-based error correction procedure

We are now prepared to outline the basic measurement-based error correction procedure. For a logical state $|\psi\rangle$ stored on n data qubits, the method is as follows:

1. Use a combination of Hadamard and CNOT gates to extract the values λ_i onto a set of ancilla qubits, $\{|a_i\rangle\}$, such that the result of Z-basis measurement of $|a_i\rangle$ represents the value λ_i.

2. Measure the ancilla qubits. The collective set of outcomes is a measurement of the syndrome.

3. Use the syndrome information to determine which Pauli error E occurred.

4. Correct the error using the appropriate unitary operator.

In practice, each of these steps has multiple caveats. Notably, the entire operation must be performed fault-tolerantly. That is, all of the circuits involved are also subject to errors and must be able to robustly accommodate errors. Fault-tolerance is discussed in the following subsection.

Furthermore, determining which error occurred (step 3) is nontrivial as a classical computation. For $n-1$ syndrome bits, there are 2^{n-1} possible syndromes, from which we must choose the most likely Pauli error from the set of 4^n possible Pauli operators. However, the 4^n Pauli operators are not uniformly likely to occur; in particular, high-weight operators are much less likely than lower weight operators that produce an identical syndrome. For a distance d code, we try to correct errors of weight w for which $2w < d$. For large d, interpreting the syndrome information is nontrivial and several decoding methods exist. In this work, the codes that we consider are all sufficiently small that syndrome decoding is relatively simple.

In step 4, it is not truly necessary to apply correction operators. Instead, it is generally sufficient to simply track errors and simply rotate the computational basis using Pauli frames [68–70]. However, in the case of measurement-free error correction this technique is not an option, since tracking the errors requires frequent syndrome measurements.

Lastly, even with fault-tolerant circuits and good decoding, failures can occur. Thus, the goal of error correction is merely to improve overall error rates. To obtain logical error rates sufficiently low for practical computation, various schemes have been proposed. One technique is concatenation, where error correction codes are layered such that the logical qubits produced at one layer become components of the logical qubits at the next level. Another option is to simply increase the code distance to improve error rates. This is most elegantly done using topological codes such as the surface code and color code and they are commonly viewed as the most realistic path forward [37–39].

Fault-tolerant computation

The circuits for syndrome extraction must be fault-tolerant. That is, errors during syndrome extraction must not propagate back to the data qubits. Similarly, logical gates between logical qubits must also be fault-tolerant, but here we are only concerned with error correction.

Here, consider a model in which gates experience error with probability p_{phys}. Then fault-tolerance demands that any single error does not propagate. Suppose all gates, including identity gates, experience error with probability p_{phys}, but that the entire circuit tolerates individual errors. Then the overall likelihood of a logical failure p_{log} grows as p_{phys}^2. Thus, for sufficiently small p_{phys}, the logical failure rate p_{log} will be less than the physical error rate p_{phys}. The value p_{th} is the error rate such that $p_{\text{log}} < p_{\text{phys}}$ for $p_{\text{phys}} < p_{\text{th}}$. This argument is formalized and generalized in a variety of theorems that guarantee the existence of threshold error rates p_{th}, such that error correction will work for sufficiently low physical noise [34, 36, 69, 71].

Pauli versus non-Pauli errors

A general unitary error E can be expanded in the basis of Pauli operators. Thus, the affected logical state $|\psi\rangle$ can also be expanded in terms of these Pauli operators. When the syndrome is measured in a Pauli basis, the state collapses onto the components whose Pauli errors match the recorded syndrome. By performing the measurement, we collapse the entire continuum of errors onto a finite set of possible errors. Therefore, error correction can deal with arbitrary errors E with sufficiently low weight. This argument does not apply for measurement-free error correction, although the result still holds. Since the entire error correction circuit is unitary, expanding in the Pauli basis is valid simply by linearity.

4.3 Example codes

Here, we review the error correction procedures for three codes. First, we look at the 3-qubit bit-flip code which corrects arbitrary single-qubit bit-flip errors. Then, we look at the related $[9, 1, 3]$ Bacon-Shor code, which corrects arbitrary single-qubit errors. Finally, we look at the $[7, 1, 3]$ Steane code, which also corrects arbitrary single-qubit errors.

The 3-qubit bit-flip code

The 3-qubit bit-flip code is the simplest example of a quantum error correction code. The logical states are

$$|0\rangle_L = |000\rangle$$
$$|1\rangle_L = |111\rangle$$

and the logical X and Z operators are $X_L = X^{\otimes 3}$ and $Z_L = Z^{\otimes 3}$. The code has two stabilizers given by

$$S_1 = Z_1 Z_2$$
$$S_2 = Z_2 Z_3.$$

Each stabilizer checks parity of two qubits. For example, S_1 has eigenvalue 1 if qubits 1 and 2 are in the same computational state, and has eigenvalue -1 if the two qubits are in opposite computational states. Ensuring that both stabilizers have eigenvalue 1 ensures that the system remains in the logical subspace. Beginning with an arbitrary state in the logical subspace, suppose that the first qubit experiences a bit-flip error. Then stabilizer S_1 will have eigenvalue -1 while S_2 remains unchanged. Similarly, if the third qubit experiences an error, only S_2 will change. However, if the second qubit is affected both stabilizers will change sign. Thus, we can associate each syndrome with a unique single-qubit error. The non-fault-tolerant circuit implementing this measurement-based procedure is shown in Fig. 4.1.

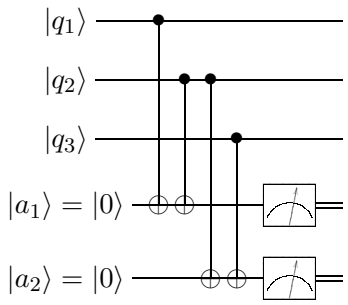

Figure 4.1: Measurement-based error correction circuit for the bit-flip code. The three data qubits $|q_i\rangle$ store the logical information. The two syndrome bits are extracted onto ancilla qubits $|a_i\rangle$. These bits are measured. Note that this circuit is not fault-tolerant.

Bacon-Shor code

The $[9, 1, 3]$ Bacon-Shor code corrects arbitrary single-qubit errors. To construct the code, we will consider the data qubits arranged in a 3×3 grid. The X and Z logical operators are $X^{\otimes 9}$ and $Z^{\otimes 9}$, respectively. This code requires only 4 stabilizers. They are

$$S_1^Z = \begin{pmatrix} Z & Z & Z \\ Z & Z & Z \\ I & I & I \end{pmatrix}, \quad S_2^Z = \begin{pmatrix} I & I & I \\ Z & Z & Z \\ Z & Z & Z \end{pmatrix},$$

$$S_1^X = \begin{pmatrix} X & X & I \\ X & X & I \\ X & X & I \end{pmatrix}, \quad S_2^X = \begin{pmatrix} I & X & X \\ I & X & X \\ I & X & X \end{pmatrix}.$$

In principle, the space is not fully defined by Z_L and the four stabilizers. Since the dimension is 2^9, we can specify up to four additional generators. However, by intentionally ignoring these degrees of freedom we introduce a convenient symmetry.

First, recall that the operators $X \otimes X$ and $Z \otimes Z$ commute since they 'anticommute' on an even number of qubits. The same holds for arbitrary X and Z type operators that overlap on an even number of qubits. Now consider the operator $X_1 X_2$ acting on the first row of the Bacon-Shor code. Clearly, this operator commutes with the X-type stabilizers. However, this operator also commutes with the Z-type stabilizers since they overlap on an even number of qubits. Thus, $X_1 \otimes X_2$ does not affect the logical state, or the syndrome.

This property holds for any pair of X operators in the same row, and also for any pair of Z operators in the same column. Collectively, these operators act on the remaining degrees of freedom, although these operators do not all commute. We can ignore these degrees of freedom by thinking of them as just a choice of gauge that is free to vary over the course of a computation. We can specify the logical states by

choosing a gauge. One choice is

$$|0\rangle_L = (|+++\rangle + |---\rangle)^{\otimes 3}$$
$$|1\rangle_L = (|+++\rangle - |---\rangle)^{\otimes 3}$$

where each term in parentheses represents a row of qubits. (This gauge is specified by choosing 4 independent operators $X_i \otimes X_j$, each acting on the same row, and fixing their eigenvalues to 1.)

As an aside, notice the symmetry between the X and Z stabilizers. This code is an example of a Calderbank-Shor-Steane (CSS) code [28, 29]. A CSS code has Z-type and X-type stabilizers, composed of tensor products of only Z, or X operators, respectively. The Z-type stabilizers are sensitive to bit-flip errors (X), while the X-type stabilizers detect phase errors (Z). The process of correcting errors can be split into separate cycles for bit-flip and phase errors with the two cycles identical up to a change of basis. Thus, to demonstrate the error correction procedure it is sufficient to discuss bit-flip errors.

Bit-flip errors are detected by the two Z stabilizers, S_1^Z and S_2^Z. Due to the gauge freedom, a bit-flip error in one row can be corrected by applying an X operator to any qubit in the same row. Thus, we see that the stabilizer structure is identical to the 3-qubit bit-flip code. The bit-flip portion of the circuit is shown in Fig. 4.2.

Steane code

The $[7, 1, 3]$ Steane code is also a CSS code and is also capable of correcting arbitrary errors, three X-type and three Z-type. Again, we will focus on bit-flip errors which are detected by the Z-type stabilizers

$$S_1 = Z_1 Z_5 Z_6 Z_7$$
$$S_2 = Z_3 Z_4 Z_6 Z_7$$
$$S_3 = Z_2 Z_4 Z_5 Z_7.$$

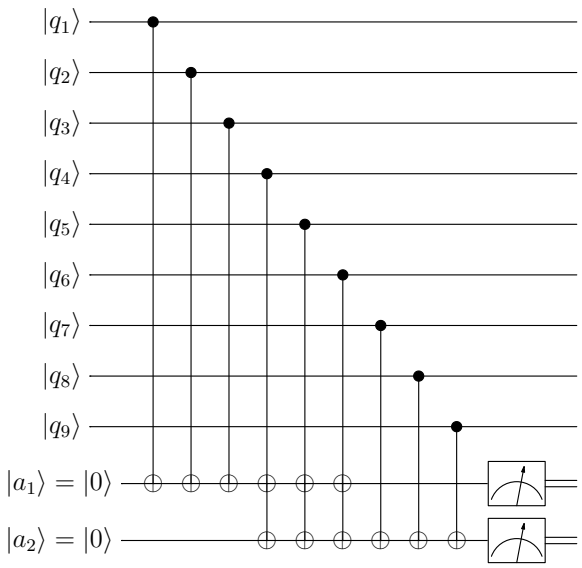

Figure 4.2: The measurement-based syndrome extraction process for the Bacon-Shor code. The ancilla qubits are measured in the final step, and the extracted syndrome is interpreted using classical computation before a correction operator is applied. Note that this circuit is not fault-tolerant.

With 3 stabilizers, there are $2^3 = 8$ possible error syndromes. One of the 8 cases corresponds to the logical subspace, leaving 7 possible syndromes indicating that an error occurred. Each of the 7 single-qubit bit-flip errors corresponds to a unique syndrome. For example, if q_1 experiences an error only S_1 is affected. Then measurement based error correction proceeds as in the previous examples—the syndrome is extracted and appropriate correction operators are applied.

4.4 Measurement-free error correction

The prominent hurdle for error correction using neutral atoms is that measurement must be avoided during computation. In the measurement-based case, the act of measurement acts as a way to remove entropy from the system. If measurement is not allowed, there must be an additional means of removing the entropy that accumulates

during a computation.

On neutral atom systems, this process is provided using qubit reset. That is, neutral atoms can reliably be reset to the logical $|0\rangle$ state with relatively low induced noise. Over the course of a coherent error correction cycle, entropy is transferred from the data qubits to the ancilla qubits and subsequently removed by resetting the ancillas. Thus, the ability to reset qubits is a crucial resource for measurement-free error correction.

Neutral atom qubits also benefit from the ability to implement $\mathrm{C}_k\mathrm{NOT}$ gates for relatively large k. Toffoli gates implement AND gates, swapping the logical state of the target qubit only if both control qubits are in the logical 1 state. Thus, Toffoli and X gates are universal for classical logic. The process of decoding error syndromes and determining the appropriate response is a classical computation, but to perform measurement-free error correction this computation must be performed on quantum hardware. The $\mathrm{C}_k\mathrm{NOT}$ gates expedite the process of implementing the required logical circuits.

The Rydberg interaction used to implement $\mathrm{C}_k\mathrm{NOT}$ gates also provides a way to perform parallel CNOT gates where a single control qubit targets multiple data qubits. The ability to implement parallel CNOT gates improves the time required for syndrome extraction. This ability is also particularly well-suited to measurement-free error correction, since the extraction process is slightly more elaborate compared to the measurement-free case, as we explain in the following subsection.

Extended set of stabilizers

In the previous examples, we specified the structure of each code by providing the stabilizers. As mentioned earlier, the term stabilizer is a slight misnomer. The given operators were stabilizer generators. Since the generators are abelian and have order 2, the set of all stabilizers generated by m generators has $2^m - 1$ nontrivial elements, ignoring possible phases. Each of these operators stabilizes the logical subspace. If stabilizer values could be extracted and processed without error the additional stabilizers would not provide additional useful information. The procedure we propose

is to copy onto ancillas the redundant information of a subset of these additional stabilizers. This enables one not only to identify data errors, but also errors that occur during syndrome extraction. The redundancy becomes useful when combined with the Toffoli and C_kNOT gates, where the quantum gates act as logical 'AND' gates to ensure that stabilizer values agree, conditionally targeting errors only if extracted stabilizer values match expected syndromes. Using this method, the ancilla qubits store only classical information—i.e., they are immune to phase errors and are not directly entangled with each other.

Measurement-free circuits

Bit-flip code

Starting with the usual stabilizers

$$S_1 = Z_1 Z_2$$
$$S_2 = Z_2 Z_3.$$

we can define the additional stabilizer

$$S_3 = S_1 S_2 = Z_1 Z_3.$$

Using the third stabilizer, it is possible to correctly identify if a single error occurs during ancilla preparation or syndrome extraction (collectively: extraction errors). This property follows from the fact that a correctly extracted syndrome always produces an even number of ancillas in the logical $|1\rangle$ state, as shown in Table 4.1. Therefore, a single extraction error occurs if an odd number of ancilla qubits occupy a logical $|1\rangle$ state. The error-correction circuit is shown in Fig. 4.3. The circuit makes use of C_3NOT gates, to correct errors on the data qubits only if the ancillary state corresponds to a valid syndrome.

An advantage of using additional stabilizer information is that the procedure does not require separate ancilla verification. That is, single-qubit extraction errors can

Table 4.1: Correctly extracted syndromes for single-qubit bit-flip errors on the logical $|000\rangle$ state. The table is easily extended to errors on the $|111\rangle$ state.

	$\|000\rangle$	$\|100\rangle$	$\|010\rangle$	$\|001\rangle$
Z_1Z_2	0	1	1	0
Z_2Z_3	0	0	1	1
Z_1Z_3	0	1	0	1

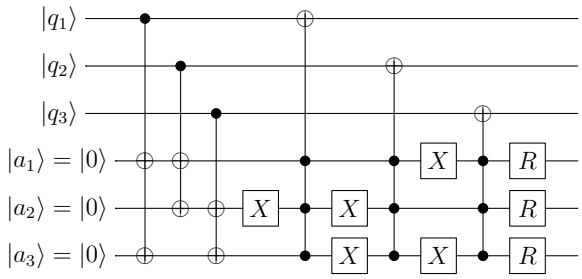

Figure 4.3: The full measurement-free extraction and correction circuit for the BF code. The first 3 gates are for syndrome extraction. The combination of X gates and C_3NOT gates detect properly extracted syndromes and correct errors accordingly. If a syndrome value is incorrectly extracted, the data qubits are not affected. Reset operations are performed in the final step, indicated with R operations. This circuit also demonstrates the bit-flip correction procedure for the BS code, taking each $|q_i\rangle$ to be a row in the BS code. Then each CNOT gate is interpreted as 3 CNOT gates, one controlled by each qubit in the row. The C_3NOT gates target any single qubit in the row. A similar procedure is required for phase errors in the BS code.

be detected simply from the combinatorics of properly extracted syndromes. In our measurement-free circuits, the C_kNOT gates act nontrivially on data qubits—i.e. correct errors—only if syndromes are properly extracted. This implies that pre-existing data errors can survive a faulty measurement-free cycle. However, with high probability the surviving data error is simply corrected during the following cycle.

Bacon-Shor code

As in the measurement-based case, the procedure to perform error correction then proceeds in a manner similar to the BF code. To correct bit-flip errors, we consider the additional stabilizer $S_3^Z = S_1^Z S_2^Z$. Like in the bit-flip code: the extended syndrome is extracted onto three ancilla qubits. The properly encoded syndromes are identical to those shown for the bit-flip code in Table 4.1. The circuit then proceeds as in Fig. 4.4, with C_3NOT gates targeting errors row-by-row. The numbering scheme in the circuit has row (123), (456), and (789). Recall that by the symmetry of the Bacon-Shor code, the C_kNOT gates correcting an error in one row by targeting any qubit in the same row. The procedure for correcting phase errors is analogous, although extraction and correction is done by column instead of by row.

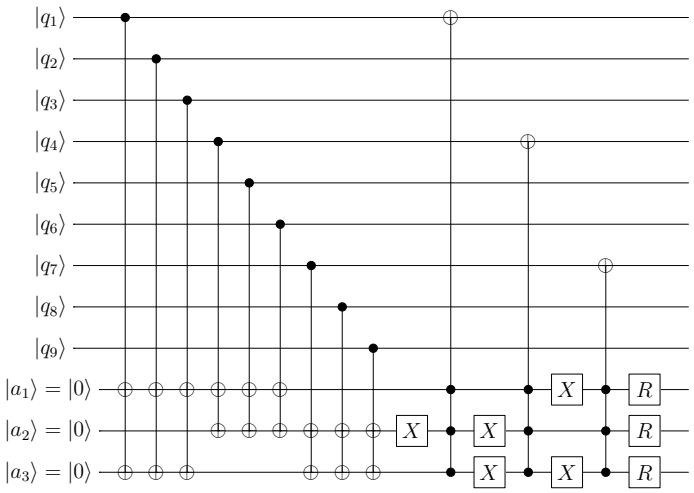

Figure 4.4: The full bit-flip error extraction and correction circuit for the BS code. The first 9 gates are for syndrome extraction, the C_3NOT gates correct the errors. Phase errors are corrected in an analogous process, but data qubits are grouped by columns instead of rows. Here, the rows are (123), (456), and (789).

Steane code

The procedure for the Steane code is slightly more complicated but also more interesting—demonstrating the potential combinatorial power of an extended set of stabilizers. Again focusing on bit-flip errors, we begin with the Z-type stabilizers

$$S_1^Z = Z_1 Z_2 Z_3 Z_7$$
$$S_2^Z = Z_1 Z_2 Z_4 Z_6$$
$$S_3^Z = Z_1 Z_3 Z_4 Z_5.$$

With 3 Z-type generators, we can form 7 distinct stabilizers. The structure of these stabilizers is shown in Fig. 4.5. This qubit-stabilizer relationship is highly symmetric. Note that each qubit affects the value of exactly four stabilizers and that any two stabilizers overlap on exactly two qubits. Furthermore, the diagram is symmetric under exchanging qubits with stabilizers.

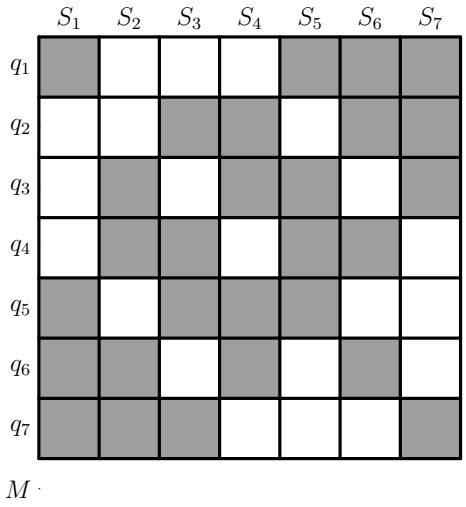

Figure 4.5: The qubit-stabilizer structure, where a shaded box indicates that the corresponding stabilizer (column) acts on the corresponding qubit (row). For Z-type stabilizers, e.g., $S_1 = Z_1 Z_5 Z_6 Z_7$. Thinking of the columns as ancillas, note that a single error on a data qubit would leave exactly four ancillas in the $|1\rangle$ state.

For error correction, all 7 syndrome bits are extracted. Each qubit affects four stabilizers, which are used as the control qubits for C_4NOT gates which target data qubits as shown in Fig. 4.6. From the relationships in Fig. 4.5 it is clear that no single-qubit error during ancilla preparation or extraction will propagate to the data. For a properly extracted single-qubit error, 4 ancilla qubits will occupy the $|1\rangle$ state. Then an improperly extracted syndrome with one error will have either 3 or 5 ancillas occupying the $|1\rangle$ state. In the 5 case, the C_4NOT gates are unaffected. A single-qubit error is insufficient to trigger an accidental C_4NOT. In the case of 3 ancillas in the $|1\rangle$ state, no C_4NOT gates will trigger; thus, the data error survives but remains correctable. With high probability, this error is simply corrected on the next cycle.

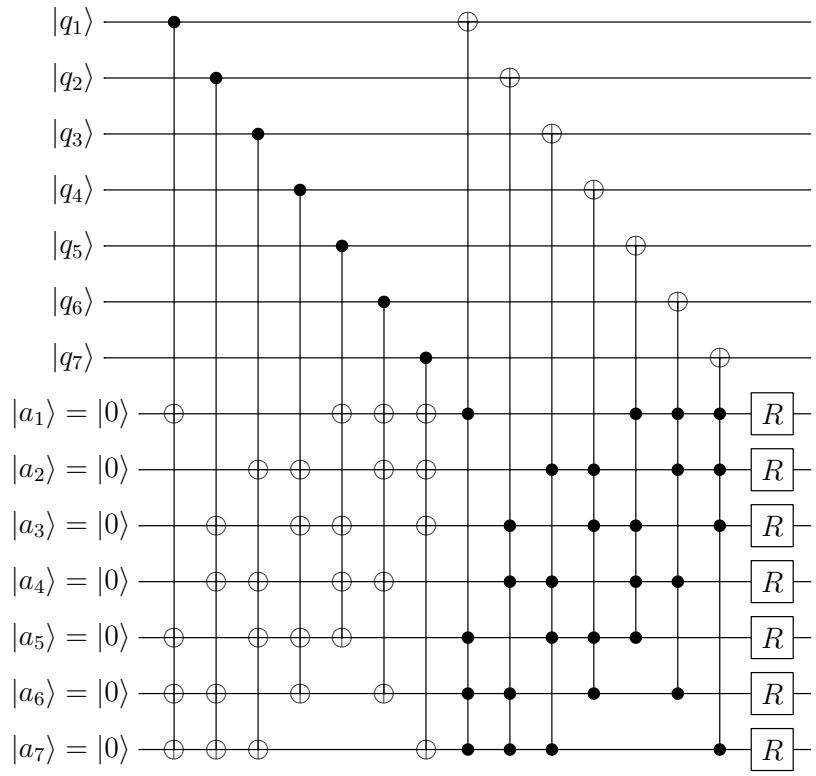

Figure 4.6: Error correction circuit for the Steane code for bit-flip errors. The circuit for phase errors is similar.

As an aside, the technique of using additional stabilizer information can also be applied in measurement-based error correction where it is potentially more powerful. In the measurement-based setting, we do not need to perfectly extract syndromes in order to correctly identify errors. From the structure of Fig. 4.5, it is clear that 3 or 5 stabilizers in the $|1\rangle$ state is sufficient to determine which data error occurred and also which extraction error occurred. Furthermore, 2 extraction errors lead to nonsensical syndromes and though the data error can not be identified, the error does not propagate. Thus, in the measurement-based setting, at least three extraction errors are required for an extraction error to reach the data.

4.5 Simulation method

We performed a numerical simulation of measurement-free error correction using the circuits shown in the previous section. We adopted an error model controlled by two error-rate parameters: the gate rate p_{gate}, and the memory (or idle-gate) rate p_{mem}. All single-qubit gate errors are assumed to be depolarizing, i.e., if an error occurs on qubit i, then a single-qubit Pauli is selected at random and applied to qubit i. For error rate p, this is represented by using the Kraus operators

$$E_i \in \left\{ \sqrt{1-p}\, I,\ \sqrt{\frac{p}{3}}\, X_i,\ \sqrt{\frac{p}{3}}\, Y_i,\ \sqrt{\frac{p}{3}}\, Z_i \right\}$$

applied for each qubit i at each time step. Two-qubit gate errors occur with the same probability p_{gate} as single-qubit gates, but the error is chosen at random from the set of 2-qubit Pauli operators. That is, for a 2-qubit gate G acting on qubits i and j, we represent this noise using the Kraus operators

$$E_i \in \left\{ \sqrt{1-p_{\text{gate}}}\, G,\ \sqrt{\frac{p_{\text{gate}}}{15}}\, G \cdot \sigma_{i_k} \otimes \sigma_{j_\ell} \right\}$$

for $(i_k, j_\ell) \neq (0, 0)$. For multiqubit gates, each control–target pair of qubits is treated as a two-qubit gate site, subject to error model as other two qubit errors. In effect, $\mathrm{C}_k\mathrm{NOT}$ gates have an error rate of roughly $k \cdot p_{\text{gate}}$, roughly matching physical error

models [65].

The simulated circuits required the ability to perform single-qubit Pauli, CNOT, and C_kNOT gates. The state evolution was performed using stabilizer simulation, in a manner similar to the techniques outlined by Aaronson and Gottesman in [72]. The C_kNOT gate is not in the Clifford group, and is not typically simulable using the Aaronson-Gottesman method. However, in every circuit studied here, the C_kNOT gates are always controlled by the ancilla qubits, which only store classical information and are modeled as classical bits. Thus, C_kNOT gates can be easily implemented.

Markovian evolution

The error model that we seek to describe is Markovian, and we can use this fact to substantially speed up the computation. We will categorize the logical state of the system into categories of error state. Recall that in coherent error correction, imperfect states can survive correction cycles, so we consider 5 possible options:

1. Logically correct
2. A single bit-flip error
3. A single-phase flip error
4. Both a bit-flip and a phase flip error
5. A logical failure

The likelihood of encountering one of these options is called the population p_k of that state. Then a single error correction cycle is given by a transfer matrix T, where entry $T_{k\ell}$ is the probability that a state beginning an error cycle in state ℓ ends in state k. They satisfy $\sum_\ell T_{k\ell} = 1$. We pessimistically assume that $T_{55} = 1$ so that a logically failed state never accidentally gets corrected. Then the populations evolve as

$$p'_k = \sum_\ell T_{k\ell} p_\ell$$

so that the full dynamics of the error correction procedure is determined by the transfer matrix.

To efficiently collect data on circuit performance, we used simulation and computational techniques similar to those in Refs. [73] and [74]. Rather than simply simulating circuits and randomly choosing errors according to the appropriate probability as the simulation proceeds, we sample the space of possible errors directly, eliminating cycles in which no errors occur.

Naïvely simulating the circuit while randomly assigning errors will encounter a logical failure with probability $p_{\log}$. Thus, the time needed to perform a simulation with fixed error rate parameters is $O(1/p_{\log})$. To generate an entire curve then requires varying the error parameter and computing $p_{\log}$ for each set of inputs. Overall, the number of total simulations required could easily be of order 10^9, particularly with multiple input parameters. Using our approach, sampling requires varying input states and fault paths, up to certain order. Estimating the coefficients $\alpha_{ijk\ell}$ requires a set of simulations for each input state and fault-type (i, j). With this method, the number of simulations required for a reasonable estimate is of order 10^5, with 2 input parameters, improving the required number of simulations by 4 orders of magnitude.

The error rates p_{gate} and p_{mem} correspond to the likelihood of an error during a gate time Δt which we take to be 1. For a circuit requiring t total time steps, there are then qt possible memory errors. Similarly, the circuit requires a variety of multiqubit gates. Each single- and two-qubit gate produces a single gate error site, while each $\mathrm{C}_k\mathrm{NOT}$ gate counts as k error sites. We take g to be the total number of gate error sites.

Now consider the possible evolutions in which i memory errors and j gate errors occur. There are $\binom{qt}{i}$ possible ways to choose the memory error sites, and $\binom{g}{j}$ ways to choose the gate error sites. Thus, the total probability of a fault path with i memory and j gate errors is

$$P(i,j) = \binom{qt}{i}\binom{g}{j} p_{\text{mem}}^{i}(1-p_{\text{mem}})^{qt-i} p_{\text{gate}}^{j}(1-p_{\text{gate}})^{g-j}. \tag{4.1}$$

Now let $\alpha_{ijk\ell}$ be the probability that a state beginning in state ℓ will end in state

k, averaged over the set of all (i, j) fault paths. Then for each entry $T_{k\ell}$, we can write

$$T_{k\ell} = \sum_{ij} \alpha_{ijk\ell} P(i, j).$$

This sum converges rapidly for $p \ll 1$, and can be truncated at low order while yielding accurate estimates for the transition probabilities. Thus, by sampling the set of possible input states, and the set of (i, j) fault paths for low i and j, we can determine the full transition matrix. Since circuits can be efficiently simulated, the entire simulation procedure is efficient and can be easily scaled to additional qubits.

To determine a single logical error rate from the transfer matrix, we can examine 4×4 submatrix of T corresponding to correct or correctable states. For each of the codes examined here, the eigenvalues of each of these matrices had 3 small eigenvalues, and one eigenvalue near one. Thus, in the correctable subspace, the logical state rapidly (i.e. within 1 or two applications of T) converged toward a state whose populations were held at fixed ratios. This correctable state then simply decayed as $(1 - p_L)^n \vec{p}$ where $(1 - p_L)$ is the largest eigenvalue of the submatrix. Thus, the effective likelihood of logical failure is p_L.

4.6 Simulation results

With the logical rates p_L in terms of the physical parameters, the threshold was evaluated by determining p_{gate} such that the logical error rate $p_{\log}$ satisfied $p_{\log}(p_{\text{gate}}) = p_{\text{gate}}$. To reduce $p_{\log}$ to a function of a single parameter, we set p_{mem} to a fixed value, or set $p_{\text{mem}} = p_{\text{gate}}$. For neutral atom qubits, memory error rates are one to two orders of magnitude below gate rates. In this region of parameter space, varying p_{mem} had little effect on the threshold gate rate, demonstrated in Figs. 4.7 and 4.8. The threshold results are summarized in Table 4.2.

The difference between the thresholds for the Bacon-Shor and Steane codes highlights the behavior of C_kNOT gates with unprotected ancilla qubits. In the Steane code, the successful correction of a data error depends on the successful extraction of 4 syndrome values, while the Bacon-Shor depends on only 3 syndrome

Table 4.2: We compare our simulated coherent (CEC) threshold values to measurement-based (MEC) gate thresholds in the literature, for $p_{\text{mem}} = 0$ and $p_{\text{mem}} = p_{\text{gate}}$. The BS and Steane measurement-based values are the best values obtained for each code in Ref. [75] (using different ancilla verification schemes). The BF value is obtained from [76] and is scaled by 1.5 since our error rate includes phase errors. All measurement-based simulations also determined first-level depolarizing thresholds.

		BF	BS	Steane
CEC	$p_{\text{mem}} = 0$	0.010	1.8×10^{-3}	8.9×10^{-5}
	$p_{\text{mem}} = p_{\text{gate}}$	5.5×10^{-4}	1.0×10^{-4}	3.2×10^{-5}
MEC	$p_{\text{mem}} = 0$		2.6×10^{-4}	5.0×10^{-4}
	$p_{\text{mem}} = p_{\text{gate}}$	~ 0.03	2.1×10^{-4}	2.6×10^{-4}

values. Furthermore, the syndrome extraction process for the Steane code requires 56 CNOT gates, compared with 36 for the Bacon-Shor code. Thus, the C_kNOT gates performing error correction are significantly more likely to fail in the case of the Steane code. However, in all procedures studied here, failures in extraction do not propagate *new* errors onto data qubits.

4.7 Discussion

Earlier work on measurement free error correction found a threshold of $p_T \approx 3.8 \times 10^{-5}$ for the 9-qubit Bacon-Shor code [61]. Thus, our work indicates a substantial improvement over this value. Additionally, the earlier value needs 18 additional ancilla qubits, while our protocol needs just 3. The differences can be attributed to the combination of extracting additional stabilizer values, coupled with the efficiency of C_kNOT gates for performing classical logic.

Directly comparing our result to measurement-based results is not particularly straightforward— measurement-based values depend on the chosen ancilla verification scheme and do not use extra stabilizer information. In addition, there is some

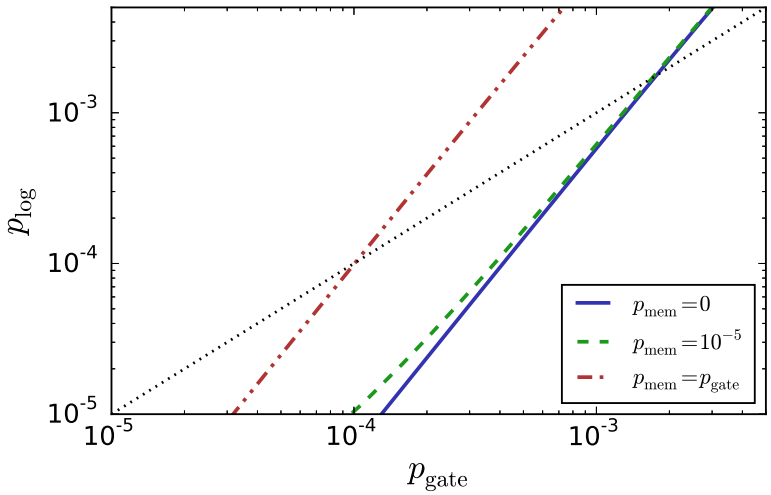

Figure 4.7: Logical error rate vs. gate error rate for the Bacon-Shor code, with three different choices of memory error rate. The dotted line shows $p_{\log} = p_{\text{gate}}$ with p_{th} where $p_{\log}(p_{\text{gate}})$ crosses the dotted line. The difference between the curves with memory rates of 0 and 10^{-5} is minimal.

arbitrariness in our choice of an error model for C$_k$NOT gates. With these caveats, in Table 4.2, we compare our results to the best measurement-based threshold values from Ref. [75], which are also first-level depolarizing thresholds. The dramatic difference in thresholds for the case of the Bacon-Shor seems to exist only in the regime where memory error rates are small. In this regime, errors are dominated by gate errors, but the circuit lengths for measurement-free error correction using neutral atom resources are typically quite small – and certainly smaller than those required for ancilla verification. Without the efficiency of multiqubit resources, we would expect thresholds to drop.

Somewhat surprisingly, the thresholds calculated for measurement-free error correction are comparable to, and, in the case of Bacon-Shor, better than thresholds calculated for measurement-based error correction. The threshold error rates are encouraging – the bit-flip and Bacon-Shor codes both yield values that are realistic for neutral atom systems [77]. The overhead required for measurement-free is not

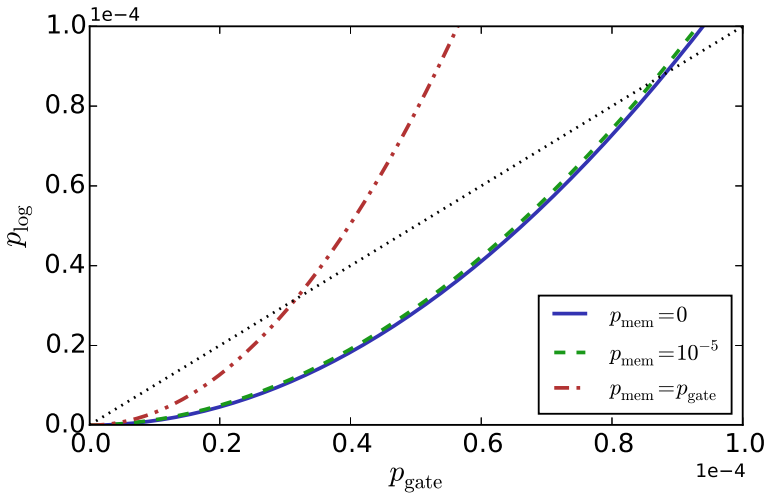

Figure 4.8: Logical error rate vs. gate error rate for the Steane code, with three different choices of memory error rate. The dotted line shows $p_{\log} = p_{\text{gate}}$ with p_{th} where $p_{\log}(p_{\text{gate}})$ crosses the dotted line. Note the near overlap between the curves with memory rates of 0 and 10^{-5}.

greater, and possibly even less than that in measurement-based, though C_kNOT gates are required.

The results demonstrate that coherent error correction is potentially a viable path towards realizing protected logical qubits, and that the topic warrants further study. In particular, a variety of questions remain about the scalability of coherent error correction techniques. The main concern for scalability is the use of additional stabilizers. Since the number of stabilizer generators grows linearly with the number of qubits, the scalability question amounts to determining how many additional stabilizers are required to see a performance gain. If the combinatorial growth of additional stabilizer information scales favorably, the use of additional stabilizer information could be a promising technique in measurement-based error correction, as well as in the measurement-free case. It would be interesting to compare thresholds between the two cases, although we save this for future work.

5 CONCLUSION

In this work, we have addressed several topics from the theory of quantum computation and information. We first discussed the geometry of entanglement. By using a mathematical result from the theory of orbitopes, we were able to approximate the set of separable quantum states. Formulating the set of separable states in terms of its orbitope structure offered insight into the geometric distinction between separable and entangled states for arbitrary numbers of qubits. This geometric structure motivates the definition of an entanglement monotone, i.e., a valid measure of entanglement.

We then examined classical models of quantum noise. Though dephasing noise is known to be classically simulable, the construction of such models is not straightforward in general. For the single-qubit case, we demonstrated an explicit construction of a classical model that realizes arbitrary dephasing noise. For two qubits, we explicitly constructed classical models for a subset of possible dephasing noise models. Lastly, we showed that depolarization is classical in arbitrary dimensions.

Finally, we discussed error correction, emphasizing measurement-free techniques motivated by neutral atom qubits. We demonstrated that an expanded set of stabilizers can be used to enhance fault-tolerance without additional machinery for ancilla verification, with or without measurement. In combination with the multiqubit logic gates that neutral atom systems can implement, we demonstrated error thresholds on the order 10^{-2}–10^{-4}. This result compares surprisingly well to measurement-based techniques, which is encouraging for the future of neutral atom computing.

By no means are any of these topics exhausted. Indeed, we will probably never provide a complete and convenient geometric description of entangled states. However, we hope that additional work from both the mathematical and physical approaches will continue to offer new insight into the nature of entanglement.

Regarding classical noise, we constructed only a small set of physical models. While explicitly constructing these tunable models is useful from a computational point of view, our results do not provide a way to easily generate classical models

directly from quantum models.

For error correction, the work can be extended in both theoretical and experimental directions. Experimentally, neutral atoms are expected to have error rates near threshold range and could potentially implement measurement-free error correction. From the theoretical point of view there remain substantial questions about the scalability of measurement-free techniques, and about the use of extra stabilizers in traditional measurement-based schemes.

The field of quantum computation and information is progressing rapidly. Theoretically, the implications span various topics in physics, mathematics, and computer science. Experimentally, substantial work remains to achieve practical quantum computation. We hope that this work contributes, in some way, to the future of these goals.

REFERENCES

[1] D. Crow and R. Joynt, Phys. Rev. A **89**, 042123 (2014).

[2] D. Crow, R. Joynt, and M. Saffman, "Improved thresholds for measurement-free error correction," (2016), arXiv:1510.08359.

[3] R. Jozsa and N. Linden, Proceedings of the Royal Society of London A: Mathematical, Physical and Engineering Sciences **459**, 2011 (2003).

[4] M. Van den Nest, Phys. Rev. Lett. **110**, 060504 (2013).

[5] I. H. Kim, Phys. Rev. Lett. **111**, 080503 (2013).

[6] M. Howard, J. Wallman, V. Veitch, and J. Emerson, Nature **510**, 351 (2014).

[7] L. M. Ioannou, Quantum Info. Comput. **7**, 335 (2007).

[8] S. Gharibian, Quantum Info. Comput. **10**, 343 (2010).

[9] A. Andai, Journal of Physics A: Mathematical and General **39**, 13641 (2006).

[10] K. Życzkowski, P. Horodecki, A. Sanpera, and M. Lewenstein, Phys. Rev. A **58**, 883 (1998).

[11] A. Barvinok and G. Blekherman, in *Combinatorial and Computational Geometry*, Vol. 52, edited by J. Goodman, J. Pach, and E. Welzl (Oxford U.P., 2005) pp. 51–85.

[12] G. Vidal, Journal of Modern Optics **47**, 355 (2000), http://www.tandfonline.com/doi/pdf/10.1080/09500340008244048 .

[13] A. O. Caldeira and A. J. Leggett, Annals of Physics **149**, 374 (1983).

[14] M. A. Nielsen and I. L. Chuang, *Quantum Computation and Quantum Information* (Cambridge U.P., 2010).

[15] U. Weiss, *Quantum Dissipative Systems* (World Scientific Publishing Co., 1999).

[16] G. Palma, K. Suominen, and A. Ekert, Proc. R. Soc. Lond., A **452**, 567 (1996).

[17] J. Helm, W. T. Strunz, S. Rietzler, and L. E. Würflinger, Phys. Rev. A **83**, 042103 (2011).

[18] L. Landau and R. Streater, Linear Algebra and its Applications **193**, 107 (1993).

[19] J. Helm and W. T. Strunz, Phys. Rev. A **80**, 042108 (2009).

[20] A. Grishin, I. V. Yurkevich, and I. V. Lerner, Phys. Rev. B **72**, 060509 (2005).

[21] H.-P. Breuer and F. Petruccione, *The Theory of Open Quantum Systems* (Oxford U.P., 2002).

[22] L. Cywiński, W. M. Witzel, and S. Das Sarma, Phys. Rev. B **79**, 245314 (2009).

[23] L. Cywiński, W. M. Witzel, and S. Das Sarma, Phys. Rev. Lett. **102**, 057601 (2009).

[24] W. M. Witzel and S. Das Sarma, Phys. Rev. B **77**, 165319 (2008).

[25] B. Abel and F. Marquardt, Phys. Rev. B **78**, 201302 (2008).

[26] P. W. Shor, Phys. Rev. A **52**, R2493 (1995).

[27] A. Steane, Proc. R. Soc. A **452**, 2551 (1996).

[28] A. M. Steane, Phys. Rev. Lett. **77**, 793 (1996).

[29] A. R. Calderbank and P. W. Shor, Phys. Rev. A **54**, 1098 (1996).

[30] C. H. Bennett, D. P. DiVincenzo, J. A. Smolin, and W. K. Wootters, Phys. Rev. A **54**, 3824 (1996).

[31] D. Gottesman, Phys. Rev. A **54**, 1862 (1996).

[32] E. Knill and R. Laflamme, (1996), arXiv:quant-ph/9608012 .

[33] P. W. Shor, in *37th Symposium on Foundation of Computing* (IEEE Computer Society Press, 1996) pp. 56–65.

[34] D. Aharonov and M. Ben-Or, SIAM Journal on Computing **38**, 1207 (2008).

[35] D. P. DiVincenzo and P. W. Shor, Phys. Rev. Lett. **77**, 3260 (1996).

[36] E. Knill, R. Laflamme, and W. Zurek, (1996), arXiv:quant-ph/9610011 .

[37] A. Yu. Kitaev, Annals Phys. **303**, 2 (2003).

[38] A. G. Fowler, M. Mariantoni, J. M. Martinis, and A. N. Cleland, Phys. Rev. A **86**, 032324 (2012).

[39] H. Bombin and M. A. Martin-Delgado, Phys. Rev. Lett. **97**, 180501 (2006).

[40] J. Chiaverini, D. Leibfried, T. Schaetz, M. D. Barrett, R. B. Blakestad, J. Britton, W. M. Itano, J. D. Jost, E. Knill, C. Langer, R. Ozeri, and D. J. Wineland, Nature **432**, 602 (2004).

[41] M. Hennrich, P. Schindler, J. T. Barreiro, T. Monz, V. Nebendahl, D. Nigg, M. Chwalla, and R. Blatt, in *CLEO:2011 - Laser Applications to Photonic Applications* (Optical Society of America, 2011).

[42] M. D. Reed, L. DiCarlo, S. E. Nigg, L. Sun, L. Frunzio, S. M. Girvin, and R. J. Schoelkopf, Nature **482**, 382 (2012).

[43] J. Kelly, R. Barends, A. G. Fowler, A. Megrant, E. Jeffrey, T. C. White, D. Sank, J. Y. Mutus, B. Campbell, Y. Chen, Z. Chen, B. Chiaro, A. Dunsworth, I. C. Hoi, C. Neill, P. J. J. O/'Malley, C. Quintana, P. Roushan, A. Vainsencher, J. Wenner, A. N. Cleland, and J. M. Martinis, Nature **519**, 66 (2015).

[44] P. Schindler, J. T. Barreiro, T. Monz, V. Nebendahl, D. Nigg, M. Chwalla, M. Hennrich, and R. Blatt, Science **332**, 1059 (2011).

[45] G. Waldherr, Y. Wang, S. Zaiser, M. Jamali, T. Schulte-Herbruggen, H. Abe, T. Ohshima, J. Isoya, J. F. Du, P. Neumann, and J. Wrachtrup, Nature **506**, 204 (2014).

[46] J. Kelly, R. Barends, A. G. Fowler, A. Megrant, E. Jeffrey, T. C. White, D. Sank, J. Y. Mutus, B. Campbell, Y. Chen, Z. Chen, B. Chiaro, A. Dunsworth, I. C. Hoi, C. Neill, P. J. J. O/'Malley, C. Quintana, P. Roushan, A. Vainsencher, J. Wenner, A. N. Cleland, and J. M. Martinis, Nature **519**, 66 (2015).

[47] D. Riste, S. Poletto, M. Z. Huang, A. Bruno, V. Vesterinen, O. P. Saira, and L. DiCarlo, Nat. Comm. **6** (2015).

[48] T. D. Ladd, F. Jelezko, R. Laflamme, Y. Nakamura, C. Monroe, and J. L. O'Brien, Nature **464**, 45 (2010).

[49] M. Saffman, T. G. Walker, and K. Mølmer, Rev. Mod. Phys. **82**, 2313 (2010).

[50] A. Fuhrmanek, R. Bourgain, Y. R. P. Sortais, and A. Browaeys, Phys. Rev. Lett. **106**, 133003 (2011).

[51] M. J. Gibbons, C. D. Hamley, C.-Y. Shih, and M. S. Chapman, Phys. Rev. Lett. **106**, 133002 (2011).

[52] D. Schrader, I. Dotsenko, M. Khudaverdyan, Y. Miroshnychenko, A. Rauschenbeutel, and D. Meschede, Phys. Rev. Lett. **93**, 150501 (2004).

[53] C. Knoernschild, X. L. Zhang, L. Isenhower, A. T. Gill, F. P. Lu, M. Saffman, and J. Kim, Appl. Phys. Lett. **97**, 134101 (2010).

[54] T. Xia, M. Lichtman, K. Maller, A. W. Carr, M. J. Piotrowicz, L. Isenhower, and M. Saffman, Phys. Rev. Lett. **114**, 100503 (2015).

[55] H. Labuhn, S. Ravets, D. Barredo, L. Béguin, F. Nogrette, T. Lahaye, and A. Browaeys, Phys. Rev. A **90**, 023415 (2014).

[56] C. Weitenberg, S. Kuhr, K. Mølmer, and J. F. Sherson, Phys. Rev. A **84**, 032322 (2011).

[57] M. Schlosser, S. Tichelmann, J. Kruse, and G. Birkl, Quantum Information Processing **10**, 907 (2011).

[58] Y. Wang, X. Zhang, T. A. Corcovilos, A. Kumar, and D. S. Weiss, Phys. Rev. Lett. **115**, 043003 (2015).

[59] I. I. Beterov and M. Saffman, Phys. Rev. A **92**, 042710 (2015).

[60] V. Nebendahl, H. Häffner, and C. F. Roos, Phys. Rev. A **79**, 012312 (2009).

[61] G. A. Paz-Silva, G. K. Brennen, and J. Twamley, Phys. Rev. Lett. **105**, 100501 (2010).

[62] C.-K. Li, M. Nakahara, Y.-T. Poon, N.-S. Sze, and H. Tomita, Quantum Info. Comput. **12**, 149 (2012).

[63] V. Nebendahl, Phys. Rev. A **91**, 022332 (2015).

[64] L. Isenhower, M. Saffman, and K. Mølmer, Quantum Information Processing **10**, 755 (2011).

[65] J. Gulliksen, D. D. B. Rao, and K. Mølmer, EPJ Quantum Technology **2**, 1 (2015).

[66] T. Monz, K. Kim, W. Hänsel, M. Riebe, A. S. Villar, P. Schindler, M. Chwalla, M. Hennrich, and R. Blatt, Phys. Rev. Lett. **102**, 040501 (2009).

[67] A. Fedorov, L. Steffen, M. Baur, M. P. da Silva, and A. Wallraff, Nature **481**, 170 (2012).

[68] E. Knill, Nature **434**, 39 (2005).

[69] P. Aliferis, D. Gottesman, and J. Preskill, Quantum Info. Comput. **6**, 97 (2006).

[70] D. P. DiVincenzo and P. Aliferis, Phys. Rev. Lett. **98**, 020501 (2007).

[71] J. Preskill, Quantum Info. Comput. **13**, 181 (2013).

[72] S. Aaronson and D. Gottesman, Phys. Rev. A **70**, 052328 (2004).

[73] S. Bravyi and A. Vargo, Phys. Rev. A **88**, 062308 (2013).

[74] D. S. Wang, A. G. Fowler, A. M. Stephens, and L. C. L. Hollenberg, Quantum Info. Comput. **10**, 456 (2010).

[75] A. W. Cross, D. P. Divincenzo, and B. M. Terhal, Quantum Info. Comput. **9**, 541 (2009).

[76] Y. C. Cheng and R. J. Silbey, Phys. Rev. A **72**, 012320 (2005).

[77] L. S. Theis, F. Motzoi, F. K. Wilhelm, and M. Saffman, (2016), arXiv:arXiv:1605.08891